

## Seas and swells throughout New Zealand

### A new partitioned hindcast

Albuquerque, João; Antolínez, Jose A.A.; Gorman, Richard M.; Méndez, Fernando J.; Coco, Giovanni

**DOI**

[10.1016/j.ocemod.2021.101897](https://doi.org/10.1016/j.ocemod.2021.101897)

**Publication date**

2021

**Document Version**

Final published version

**Published in**

Ocean Modelling

**Citation (APA)**

Albuquerque, J., Antolínez, J. A. A., Gorman, R. M., Méndez, F. J., & Coco, G. (2021). Seas and swells throughout New Zealand: A new partitioned hindcast. *Ocean Modelling*, 168, Article 101897. <https://doi.org/10.1016/j.ocemod.2021.101897>

**Important note**

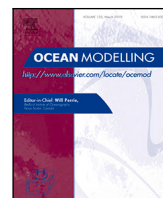
To cite this publication, please use the final published version (if applicable). Please check the document version above.

**Copyright**

Other than for strictly personal use, it is not permitted to download, forward or distribute the text or part of it, without the consent of the author(s) and/or copyright holder(s), unless the work is under an open content license such as Creative Commons.

**Takedown policy**

Please contact us and provide details if you believe this document breaches copyrights. We will remove access to the work immediately and investigate your claim.



## Seas and swells throughout New Zealand: A new partitioned hindcast

João Albuquerque<sup>a,\*</sup>, Jose A.A. Antolínez<sup>b</sup>, Richard M. Gorman<sup>c</sup>, Fernando J. Méndez<sup>d</sup>, Giovanni Coco<sup>a</sup>

<sup>a</sup> School of Environment, University of Auckland, 23 Symonds Street, Auckland, New Zealand

<sup>b</sup> Department of Hydraulic Engineering, Faculty of Civil Engineering and Geosciences, Delft University of Technology, Delft, Netherlands

<sup>c</sup> National Institute of Water and Atmospheric Research, Gate 10 Silverdale Road Hillcrest, Waikato, New Zealand

<sup>d</sup> Departamento de Ciencias y Técnicas del Agua y del Medio Ambiente, E.T.S.I de Caminos, Canales y Puertos, Universidad de Cantabria, Avda. de los Castros, s/n, 39005 Santander, Spain

### ARTICLE INFO

#### Keywords:

Hindcast  
Wind-sea waves  
Swell waves  
Wave partitions  
Multimodal spectra  
Downscaling

### ABSTRACT

A high resolution partitioned wave hindcast of New Zealand waters is presented together with validation results against 9 buoy deployments that are representative of the local wave climate. An analysis of integrated and partitioned mean wave parameters was conducted together with a study of the correlation between wave height anomalies and atmospheric indices. A directional spatial analysis was also performed to identify and quantify wave systems that are not detectable by *in situ* buoys or hindcast integrated parameters. The presented study outlines a framework of how partitions can be analyzed in order to improve our understanding of the local wave climate in terms of wind-sea and swell waves.

### 1. Introduction

Long term statistics of wave conditions (wave climate) are widely used for near/offshore research and engineering. Studies of beach morphodynamics, sediment transport and air/sea interactions, the design of marine structures, and ship routing for transport and commerce activities are examples of applications that rely on knowledge of the wave climate. As these studies and activities can be of relevant impact to the economy, urban planning, risk assessment and human lives, the need for reliable wave climate data is evident. Wave data is usually sourced from instruments such as *in situ* offshore buoys, satellite altimeters and visual records from voluntary observation ships (VOS), or estimated by numerical simulations (wave hindcasts and reanalyses). However, the aforementioned instrumental measurements have inherent issues: buoy data only represent the local wave climate, are not widely available and may either be too short or contain gaps; satellite altimeter data is only available at each satellite pass, require reprocessing to correct bias from different missions and may suffer interference from clouds, ice and land, the latter lasting up to 50 km offshore (Tournadre et al., 2009; Shanias et al., 2014; Sepulveda et al., 2015). Finally, VOS data have an accuracy of 0.5 m for wave height (Grigorieva and Badulin, 2016), which may not be suitable for some studies, and are usually restricted to known ship routes, leaving the remaining areas almost uncovered (Challenor et al., 2006). As wave hindcasts are numerical simulations, their downsides are the limitations inherent to all models, i.e. simplification of physics, equations that are not capable

to fully represent the modeled phenomena, errors in the input data, etc. Hence, validation of model results against field observations is always required. Nevertheless, due to their relative cost-effectiveness and the ability to fill the temporal and spatial gaps that exist among the available instrumental data, wave hindcasts have been widely adopted as a source of wave climate data.

Various local (Gorman et al., 2003b) and global (Reguero et al., 2012; Rascle et al., 2008) scale hindcasts have been published and investigated. Also, a number of studies comparing results from different wave models (Hanson et al., 2009; Caires et al., 2004) and wind reanalysis forcings (Lavidas et al., 2017), as well as methods to correct hindcasts' inaccuracies (Albuquerque et al., 2018; Cavaleri and Scavo, 2006; Mínguez et al., 2011) are available in the literature. Other examples of research based on hindcasts include the description of global and regional wave climate along with its short and long term trends (Cox and Swail, 2001; Semedo, 2018). Finally, wave simulations and hindcasts were used in a number of studies related to crossing seas, freak waves and ship accidents (Toffoli et al., 2011, 2005; Støle-Hentschel et al., 2020).

New Zealand, which is exposed to waves from many wave generation basins (i.e., Indian, Southern and Pacific oceans and Tasman Sea), has a multimodal wave climate that has been studied using *in situ* visual and buoy observations (Pickrill and Mitchell, 1979), local wave hindcasts (Laing, 1993; Gorman et al., 2003a,b) and satellite data (Laing, 2000). Other studies based on global wave hindcasts used synoptic patterns (Coggins et al., 2015), atmospheric oscillation modes

\* Corresponding author.

E-mail address: [j.dealbuquerque@auckland.ac.nz](mailto:j.dealbuquerque@auckland.ac.nz) (J. Albuquerque).

(Godoi et al., 2016) and a combination of both plus satellite data and statistical downscaling (Rueda et al., 2019) to explain the wave climate of New Zealand waters. Among the findings, there is an agreement that the most energetic waves reach the south and southwest coasts of the country while the east and northern coasts receive gradually less wave energy due to sheltering effects and limited fetch distances against the dominant southwesterly wave direction. An overall trend of wave height increase was found from 1958 to 2001 (Godoi et al., 2016; Cox and Swail, 2001), possibly related to an intensification of the Southern Annular Mode (SAM) (Godoi et al., 2016; Young et al., 2012; Wentz et al., 2007). Other atmospheric indices found to modulate the waves throughout New Zealand are the Southern Oscillation Index (SOI), Indian Ocean Dipole (IOD), Zonal Wave-number-3 Pattern (ZW3) (Godoi et al., 2016) and the Madden-Julian Oscillation (MJO) (Fauchereau et al., 2016).

Despite the contributions from previous research, all the hindcasts conducted and used in the aforementioned studies represent the wave spectra as an integrated set of bulk wave parameters such as significant wave height, mean period and mean wave direction ( $H_s$ ,  $T_m$  and  $\theta_m$  respectively). Although this unimodal representation fits the cases where the sea state is composed of a single wave system, it is not suitable to represent the complex multimodal wave systems (Snodgrass et al., 1966) that are present in the open ocean and even in relatively small enclosed wave generation basins (Semedo et al., 2009, 2015; Portilla-Yandún, 2018), which is also true for New Zealand. This means that integrated parameters are not always suitable to represent the specific wave systems that caused the changes in wave height or direction observed in previous studies.

In order to overcome this limitation, recent versions of wave models – i.e., WAVEWATCH III (Tolman et al., 2009) and SWAN (Booij et al., 1999) – have incorporated a spectral partitioning algorithm (Hanson and Phillips, 2001) that identifies the distinct wave systems present in the wave spectra and saves the integrated parameters of each system into separate partitions of wind-sea and swells. This approach offers a fair trade-off between preserving most of the spectral information available and the need for additional computational and storage resources. Portilla et al. (2009) also explored the wave spectrum partitioning algorithm and applied it to the ERA-Interim reanalysis' wind wave hindcast, providing an atlas of the global signature of the wave spectra (Portilla-Yandún, 2018).

Wave data from spectral partitioning provides more insightful and comprehensive information to the scientific community and is progressively being adopted in new studies, such as hindcast wave height correction (Albuquerque et al., 2018), improvement of statistical downscaling (Rueda et al., 2017) and wave climate studies in simple settings like the Black Sea (Vledder and Akpınar, 2017). However, an investigation on how a partitioned hindcast can benefit the wave climate analysis of a complex island setting is yet to be done. New Zealand is a very convenient area for this kind of study due to the diverse wave generation areas this country is exposed to, and the fact that the latest validated hindcast published for the New Zealand waters dates back to 2003 (Gorman et al., 2003a,b). Hence, this study aims to (i) present a high resolution partitioned wave hindcast for the New Zealand waters (ii) describe the data and methods used to obtain and validate such a hindcast, (iii) provide a wave climate analysis that complements the latest studies on this subject, and (iv) demonstrate the potential of the present hindcast in broadening our understanding of the wave climate of New Zealand — or any other area where this type of data is available.

The remaining of the paper is organized as follows: Section 2 describes the data used in this study while the methods employed to generate and analyze our hindcast are outlined in Section 3. Section 4 explores the wave climate analysis under the wind-sea and swells perspective. The findings are discussed in Section 5, and the final remarks are shown in Section 6.

## 2. Data

### 2.1. Offshore wave hindcast

The regional wave climate dataset presented and studied in this work was forced with boundaries from a global 20-year (1993–2012) partitioned wave hindcast (Rascle et al., 2008; Rascle and Ardhuin, 2013) provided by IFREMER (Institut Français de Recherche pour l'exploitation de la Mer), IFRhc hereinafter. The IFRhc was conducted using the WAVEWATCH III (WW3) model version 4.04, with the TEST451 (ST4) parametrization (Rascle and Ardhuin, 2013; Stopa et al., 2016a) and CFSR (Climate Forecast System Reanalysis) wind forcing. The wave spectra are discretized in 24 directional bins and 31 frequencies, the latter exponentially distributed from 0.037 Hz to 0.7 Hz. Each IFRhc point, available in a 0.5° spatial resolution, provides 3-hourly time series of integrated and partitioned wave parameters. While the integrated wave parameters consist of the commonly used estimates of significant wave height ( $H_s$ ), energetic period ( $T_e$ ) and mean wave direction ( $\theta_m$ ) among others, the partitioned wave parameters provide estimations of the equivalent variables, for up to six individual wave systems in a sea state. For instance, for a given partition  $n$ , the parameters of significant wave height, peak wave period and peak wave direction ( $\{H_{pn}, T_{pn}, \theta_{pn}; n = 1, \dots, 6\}$ , respectively) would be available. The 1st partition is reserved for the wind-sea waves ( $p1$  hereinafter) whilst the remaining five partitions ( $p2$ ,  $p3$ ,  $p4$ ,  $p5$  and  $p6$ ) refer to the simultaneous swell waves found in the sea state, ordered from higher to lower wave height. The points of the IFRhc used as boundary forcings were selected within the perimeter from 164.5°E to 181.0°E in longitude, and from 31.5°S to 50.0°S in latitude, as per Fig. 1. No spectral data is available along this area, hence partitioned wave parameters were used.

### 2.2. Bathymetry

Water depth and the shape of the seabed play an important role over the physical processes that occur with the waves as they propagate onshore. Hence, a bathymetric database that can accurately represent the features of the ocean floor is of great importance for wave modeling. The bathymetry used in this study is provided by the National Institute of Water and Atmospheric Research (NIWA). This 250 m resolution database is a compilation of multibeam and single-beam data surveys by NIWA and Land Information New Zealand (LINZ), together with international surveys performed by vessels from United States of America, France, Germany, Australia and Japan (Mitchell et al., 2012).

### 2.3. Winds

In order to account for the local wind effects on wave generation and propagation, the same wind forcings from CFSR used in the offshore hindcast were used in our simulations. The wind fields from CFSR have a spatial resolution of 0.312° from 1979 to 2009 and 0.205° from 2010 onwards, with a temporal resolution of 1 h. It should be noted that the wind database used in this study has different biases (Rascle and Ardhuin, 2013; Chawla et al., 2013) and a higher temporal and spatial resolution compared to the wind fields used previously (Gorman et al., 2003a,b; Godoi et al., 2016, 2017). While the effects of such differences will be discussed in Section 5, further details on the implementation of the CFSR reanalyses can be found in Saha et al. (2010, 2014).

### 2.4. Buoy data

From 1976 onwards, a number of buoys were moored and operated in New Zealand by private and public companies. As a result, NIWA has a compilation of wave buoy records from 13 deployments on different locations and periods of time (Fig. 1). From all deployments, 10 can potentially be used for validation as they occurred during the hindcast time-span (Table 1), yet one of the 10 deployments (Hokitika) was left aside for being too short (~2-month) for our purposes.

**Table 1**

Details of buoy deployments throughout New Zealand used for hindcast validation (except for Hokitika). Rows display the details for each deployment, columns show the site name, location, geographic coordinates, time series start/end dates and depth. Records containing directional parameters are marked with '✓', records without directional parameters are indicated with '–'.

Site	Island & coast	Latitude	Longitude	Series start	Series end	Depth (m)	$\theta$
Maunganui Bluff, Northland	North Island, W	–35.55	173.32	07/06/2006	24/07/2007	50	✓
Taharoa, Waikato	North Island, W	–38.17	174.68	07/03/1996	31/12/2000	23	–
Hokitika, West Coast	South Island, W	–42.64	170.83	21/09/1996	30/11/1996	104	–
Mokohinau I., Hauraki Gulf	North Island, NE	–35.88	175.08	30/04/1998	10/06/2004	100	✓
Mangawhai, Hauraki Gulf	North Island, NE	–36.11	174.64	14/03/1995	07/11/1997	30	✓
Katikati, Bay of Plenty	North Island, NE	–37.42	176.05	28/02/1991	31/12/1994	34	✓
Pukehina, Bay of Plenty	North Island, NE	–37.70	176.62	22/09/2003	31/01/2013	100	✓
Baring Head, Wellington	North Island, S	–41.40	174.85	03/08/1998	present	45	–
Golden Bay, Tasman	South Island, N	–40.68	172.92	16/09/2007	10/06/2008	30	–
Banks Peninsula, Canterbury	South Island, E	–43.76	173.33	06/02/1999	present	76	✓

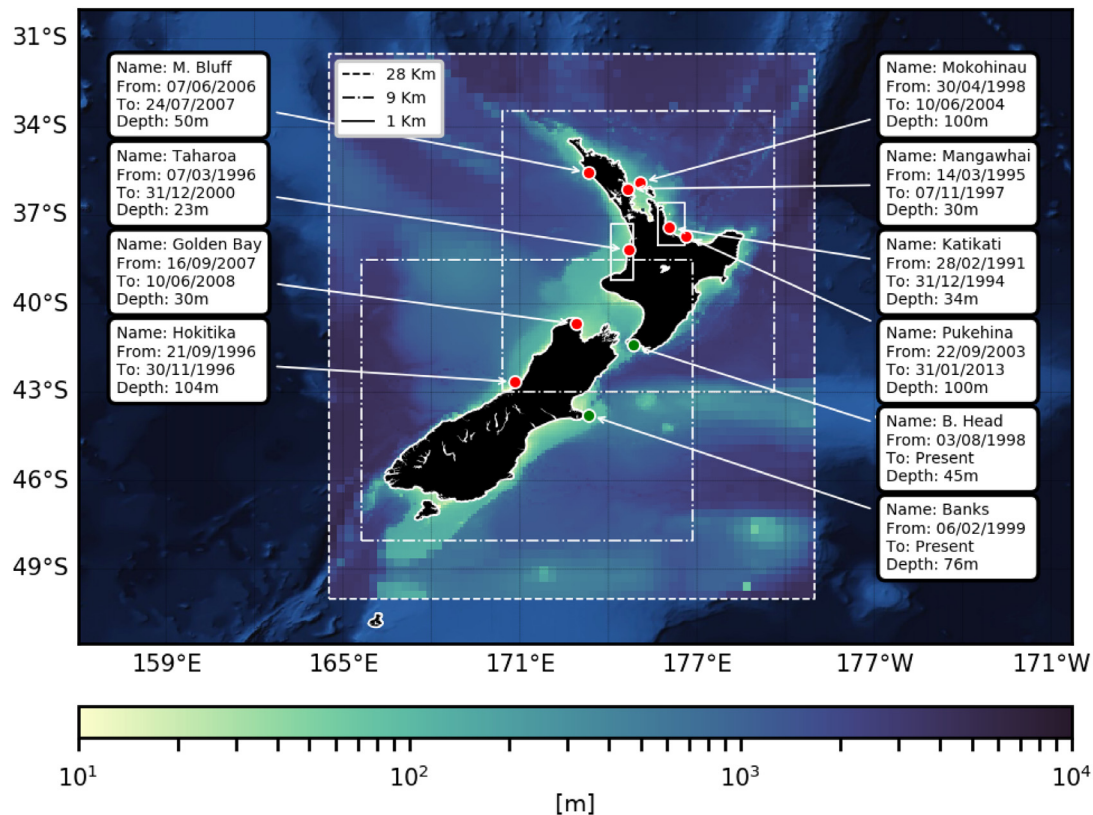


**Fig. 1.** Bathymetry surrounding New Zealand overlaid with some of the grids used for downscaling in this study. The line style of each grid indicates its resolution. Red and green dots respectively display discontinued and ongoing buoy moorings that have been used to validate our results. Textboxes show details of each deployment.

**2.5. Climate indices**

Three atmospheric indices known to affect the wave climate of New Zealand (Rueda et al., 2019; Godoi et al., 2016; Gorman et al., 2003a) were used in this study, the Southern Oscillation Index (SOI) (Chen, 1982), the Southern Annular mode (SAM) (Gong and Wang, 1999) and the Dipole Mode Index (DMI) (Saji et al., 1999). The SOI is characterized by the anomaly on the observed sea level pressure (SLP) along the western and eastern tropical Pacific, measured between Tahiti and Darwin (Australia). Its positive phase, related to abnormally high SLP across the eastern tropical Pacific (and abnormally low SLP along the western tropical Pacific), corresponds to La Niña events, which increases the occurrence of northeasterly winds in this area. The negative phase of the SOI shows opposite characteristics of SLP as well as southwesterly winds along the same area, evidencing El Niño events (Gordon, 1986). The SAM, also known as Antarctic Oscillation Index, is the difference of zonal mean SLP between 40°S and 65°S. The positive phase of this index influences the regional climate of New Zealand causing an easterly wind anomaly during summer and

a northeasterly (northwesterly) wind anomaly along the North Island (South Island) during the austral winter (Kidston et al., 2009). An increased frequency of tropical cyclones undergoing extra-tropical transition is also observed near New Zealand during the positive phases of the SAM (Diamond and Renwick, 2015). Also known as Indian Ocean Dipole (IOD), the Dipole Mode Index is characterized by sea surface temperature (SST) anomalies in the western and eastern Indian Ocean. The positive phase of the IOD implies a positive SST anomaly in the western Indian Ocean and a negative SST anomaly in eastern Indian ocean, which weakens (enhances) the storm-track over northern (southern) New Zealand during the austral winter, while the opposite occurs during negative IOD phases (Ashok et al., 2007; Griffiths, 2011).

The monthly values of the Southern Annular mode we analyzed were sourced from the British Antarctic Survey (BAS). The monthly time series of the Southern Oscillation Mode and the Dipole Mode Index were obtained from the Physical Sciences Laboratory (PSL) of the National Oceanic and Atmospheric Administration (NOAA).



### 3. Methods

#### 3.1. Wave height correction and spectral reconstruction of boundary forcing

In situ wave measurements are scarce along the Southern Ocean (Hemer et al., 2010), which prevented us to directly assess the accuracy of our boundary forcings. In order to address this shortcoming, each boundary point of the IFRhc had its wave height corrected for the whole 20-year (1993–2012) time series. The wave height correction method (Albuquerque et al., 2018) is based on satellite altimeter data and provides a set of directional calibration coefficients for the wind-sea and swell wave systems at each point along the grid boundaries. This technique is buoy independent, therefore worldwide applicable, and has been designed specifically for partitioned wave hindcasts.

The percentage of improvement in  $H_s$  accuracy obtained for each boundary point was calculated using the normalized root mean squared error (NRMSE) and the mean absolute error (MAE) before and after the correction. The results were summarized by grouping the boundary points according to the grid side they belong to, i.e. west side (from 50.0°S to 31.5°S at 164.5°E), north side (from 164.5°E to 181.0°E at 31.5°S), east side (same latitudes as north side, but at 181.0°E) and south side (same longitudes as north side, but at 50.0°S). Further details regarding the databases used, model implementation and accuracy improvements of other points can be found in Albuquerque et al. (2018).

The (up to) six corrected wave systems, available in the sea states of each boundary point, were used to reconstruct the multimodal spectral forcings of our downscaling model. For the spectral reconstruction, we used the JONSWAP spectral model (Hasselmann et al., 1973) to represent each partition as a spectral peak. The values used for the peak-width parameter ( $\sigma$ ) were the defaults (i.e.,  $\sigma_a = 0.07$  and  $\sigma_b = 0.09$ ) while the peak enhancement factor ( $\gamma$ ) was calculated based on the wave height and peak period (as per Torsethaugen et al. (1984), Haver and Nyhus (1986)) for each partition. The resulting two-dimensional spectrum (i.e., sum of the spectral representation of all partitions) was reconstructed using 40 frequencies, non-linearly distributed from 0.03 to 1.0 Hz, and 72 directional bins.

#### 3.2. Downscaling

In order to properly represent the physical processes that occur as deep-water waves propagate in shallow waters, a finer resolution grid and a nearshore wave model must be employed. In this study, we used the SWAN model (version 41.31 A) with bottom friction activated and its standard parameterizations, which includes the same swell dissipation as the IFRhc.

The boundary and wind forcing described in the previous sections were used in a 4-level (28 km, 9 km, 3 km and 1 km) set of nested grids, not all of them shown in Fig. 1, for the sake of simplicity. The 28 km grid was employed to provide the same conditions of spectral propagation from the outermost boundaries to the 9 km grids, minimizing the bias on the wave parameters of the overlapping areas of these grids. Intermediary 3 km spatial resolution grids (not shown) were nested between the 9 km and 1 km grids in order to better resolve the nearshore processes without adding much to the total computational effort. The 1 km grids shown in Fig. 1 were downscaled for model validation against the Taharoa and Katikati stations, and the nearshore study of three different areas: Raglan (west coast of New Zealand), Tairua and Tauranga (both deployments located in the northeast coast of New Zealand). Five other locations (grids not shown) were also downscaled to 3 km and 1 km in order to compare the hindcast with the Mokohinau, Mangawhai, Pukehina, Baring Head, Banks, Golden Bay and Maunganui Bluff buoys. The Hokitika area was not downscaled as its buoy time-series was deemed too short (~2-month) for our purposes.

The wave spectra were discretized in 72 directions and 34 frequencies from 0.03 to 1.0 Hz. A cut-off frequency of 0.5 Hz was applied

to the model's output, narrowing down the simulation results to a range of frequencies closer to where buoy results can be trusted (Rascle et al., 2008). The 20-year non-stationary simulation was run as 40 “embarrassingly parallel” (i.e., a small effort was required to compute each run independently of the others) 6-month SWAN runs. In order to achieve this, a stationary computation was used to define the initial state of the first 6-month non-stationary simulation. The other 39 non-stationary runs were started 36 simulation-hours earlier than their first output cycle, allowing the wave energy to propagate from the boundaries towards the whole grid. This approach was validated by comparing the final values of a simulation with their corresponding values (in time) of the next simulation along 9 different locations and several simulation transitions (not shown). The 36-hour spin-up time allowed for an homogeneous transition between the results found at the beginning of a simulation and the end of the previous one, regardless of the order they were computed. The same “warm-up” approach was applied to the nested grids, however each of these grids was still dependent on the run of their “parent” simulations. The results obtained from all the 475 SWAN runs were stored as integrated and partitioned wave parameters, and the 9 km resolution datasets were made freely available at [www.coastalhub.science/data](http://www.coastalhub.science/data).

#### 3.3. Validation

The hindcast wave parameters were validated against buoy records. The parameters presented in this study were narrowed down to those available on the majority of the New Zealand buoys — wave height ( $H_s$ ), second order period ( $T_{m02}$ ) and mean direction ( $\theta_m$ ) (or peak direction,  $\theta_p$ , depending on the equipment). The validation metrics calculated for each parameter were root mean squared error (RMSE), normalized root mean squared error (NRMSE), BIAS and Pearson's correlation index ( $r$ ). Buoy records available at a frequency higher than the model output cycle (3-hourly) were averaged before comparison. Abnormally high (spikes), low or physically impossible values were removed from the buoy dataset. Finally, we assessed the effects of the different grid resolutions (9 km, 3 km and 1 km) on the accuracy of the hindcast parameters.

#### 3.4. Wave climate analysis and data inspection

The database here presented was analyzed in three different ways. The first was a spatial analysis of integrated and partitioned wave parameters, the second was a time-series analysis of wave height parameters along six different locations off the coasts of New Zealand, and the third was a direction-based spatial analysis of partitioned parameters of wave height.

##### 3.4.1. Spectral partitioning

As the wave climate analysis in this work is based on wind-sea and swell waves, it relies heavily on spectral partitioning. It is important therefore to briefly clarify how this method works and what thresholds are used by wave models while partitioning the wave spectrum. The Hanson and Phillips (2001) algorithm identifies wave systems (local energy peaks) in the 2D wave spectrum, classifying/partitioning these peaks as wind-sea when they are actively being forced by the current winds, and swells when these peaks propagate independently of the wind. The classification is based on the wave age criterion ( $\beta$ ), i.e., the relationship between the wave phase speed and the component of the wind velocity in the wave propagation direction (please refer to equation 4 and figure 2 of Hanson and Phillips (2001) for details). While a reference value of  $\beta = 1.5$  is presented by Hanson and Phillips (2001), the WW3 and SWAN wave models use a standard value of  $\beta = 1.7$ . However, as models parameterizations seem to reflect in both the higher and lower frequencies of the wave spectra (Stopa et al., 2016b), the characteristics of the partitioned wave systems may vary between each model. It should be noted that, within this method, wave

systems propagating independently of the wind are classified as swells, regardless of other characteristics these systems may have. The same occurs while identifying wind-seas, i.e., wave systems being actively forced by the winds. Hence, it is possible to find minimum values of peak period around 1 s in swell systems, as well as maximum periods of ~28 s for wind-sea waves — as opposed to frequency-based methods of wind-sea and swell waves partitioning, which identify each wave system using a frequency threshold (Wang and Hwang, 2001; Violante-Carvalho et al., 2002). Finally, while WW3 provides up to 6 partitions ( $p1$  to  $p6$ ), it is possible to configure SWAN to output up to 10 partitions ( $p1$  to  $p10$ ). Both models organize the output partitions in the same way (i.e.,  $p1$  is the wind-sea partition and the remaining partitions are reserved for swells, ordered from highest to lowest wave height).

### 3.4.2. Spatial analysis of integrated and partitioned wave parameters

The spatial analysis here presented includes mean and seasonal mean (vector averaged for wave direction) of partitioned and integrated wave parameters. Integrated wave parameters studied include  $H_s$ , extreme values of  $H_s$  (mean of the top 1%  $H_s$ ,  $H_s^{99}$  hereinafter),  $T_{m02}$  and  $\theta_p$ . Partitioned wave parameters constitute of  $H_s$ ,  $H_s^{99}$ ,  $T_p$  and  $\theta_p$  for each wave system (SWAN was set to output 1 wind-sea and 5 swell wave partitions) plus an aggregated swells partition ( $\{H_{pn}, H_{pn}^{99}, T_{pn}$  and  $\theta_{pn}; n = 1, \dots, 6, \text{swell}\}$  where  $n$  represents the partition number,  $p1$  is the sea partition,  $pswell$  is the aggregated swell partition and  $\{H_{pn} > H_{pn+1}; n = 2, \dots, 5\}$ ). The analysis of partitioned parameters was done for wind-sea ( $p1$ ), swells ( $pn; n = 2 \dots 6$ ) and aggregated swell ( $pswell$ ) waves.

Aggregated swell statistics of wave height were calculated by root squaring the sum of the squares of the wave heights of each swell partition (Eq. (1)):

$$H_{pswell} = \sqrt{\sum_{n=2}^6 H_{pn}^2} \quad (1)$$

peak swell period ( $T_{pswell}$ ) of each sea state was defined as the peak period of the swell system with the largest wave power (Eq. (2)):

$$T_{pswell} = T_{pi}, \text{ where } i = \text{index}(\max(T_{p2} \cdot H_{p2}^2, T_{p3} \cdot H_{p3}^2, \dots, T_{p6} \cdot H_{p6}^2)), \{i = 2, \dots, 6\} \quad (2)$$

and peak swell direction ( $\theta_{pswell}$ ) was also calculated based on the wave power of the available swell systems (Eq. (3)):

$$\theta_{pswell} = \text{atan2} \left( \frac{\sum_{n=2}^6 H_{pn}^2 \cdot T_{pn} \cdot \cos(\theta_{pn})}{\sum_{n=2}^6 H_{pn}^2 \cdot T_{pn} \cdot \sin(\theta_{pn})} \right) \quad (3)$$

When presenting statistics of  $H_{pn}$ , we also provided information on how much of the total wave height this partition represents with respect to  $H_s$  (i.e.,  $\alpha_{pn}$ ) by dividing the square of  $H_{pn}$  by the square of  $H_s$  as per Eq. (4):

$$\alpha_{pn} = \frac{H_{pn}^2}{H_s^2}, \quad \{n = 1, \dots, 6\}. \quad (4)$$

When working with partitioned data, a few issues regarding mean values emerge while dealing with pure wind-seas and pure swells sea states, as well as extreme events. Therefore, in order to address such issues, two different definitions of mean and extremes were necessary:

- mean: the sum of the wave parameter values divided by the number of occurrences of such parameter (i.e., wave height is different than 0) along the 20-year time series;
- mean contribution: the sum of the wave parameter values divided by the number of model outputs along the 20-year time series;
- integrated extreme mean: the mean of the events above the 99th percentile threshold of an integrated parameter;

- partition/sector extreme mean: the mean of the events above the 99th percentile threshold of a partitioned/sectorized parameter, regardless of the integrated 99th percentile threshold of the same parameter.

For integrated parameters, mean and mean contribution are the same. However, parameters of wind-sea and swell partitions present different values of mean compared to the mean contribution, as these systems are not always present. Therefore, information regarding the mean wave height of wind-sea and swells is complemented by the mean contribution of each of these systems in the total  $H_s$ , expressed in terms of  $\alpha$  (Eq. (4)). Partitioned parameters of wave direction and peak period were calculated only as mean.

Areas of crossing, opposing and following seas were also defined throughout the study area, along with their respective percentage of occurrence. In terms of direction, the areas were defined as per Toffoli et al. (2005), i.e., crossing, opposing and following seas occur when an angle of  $90^\circ/270^\circ \pm 30^\circ$ ,  $180^\circ \pm 30^\circ$  and  $0^\circ \pm 30^\circ$ , respectively, is present between two wave systems. The wave height criterion used in this study is that both systems'  $H_s$  must be larger than 1 m. No restrictions were applied to wave period or whether the wave system was a wind-sea or a swell. As we used up to 6 partitions per sea state, the selection method eventually found more than one pair of wave systems under the crossing/opposing/following condition per sea state. Nevertheless, it only mapped whether these events occurred or not, i.e., no information on the number of associated sea states was provided.

### 3.4.3. Wave height annual variability

Values of mean annual variability (MAV) and inter-annual variability (IAV) (Stopa et al., 2013) were computed for integrated (bulk) and partitioned wave height parameters. The MAV is the average of the annual standard deviation normalized by the annual average, and measures the variability of a parameter  $x$  (e.g., wave height) within each year over a period of  $m$  years, assuming that each year has  $n$  records of  $x$  (Eq. (5)).

$$\text{MAV} = \frac{1}{m} \sum_{j=1}^m \sqrt{\frac{1}{n} \sum_{k=1}^n \left( x_{jk} - \left( \frac{1}{n} \sum_{k=1}^n x_{jk} \right) \right)^2} \left( \frac{1}{n} \sum_{k=1}^n x_{jk} \right)^{-1} = \overline{\left( \frac{\sigma_j}{\bar{x}_j} \right)} \quad (5)$$

Where  $j$  and  $k$  are indices for the year and record respectively,  $\sigma$  is the standard deviation, and the overbar stands for average. The IAV is defined as the standard deviation of the annual means, normalized by the overall mean, as per Eq. (6), and measures the variability of the parameter  $x$  within the years, over  $m$  years, with  $n$  yearly records:

$$\text{IAV} = \sqrt{\frac{1}{m} \sum_{j=1}^m \left[ \left( \frac{1}{n} \sum_{k=1}^n x_{jk} \right) - \left( \frac{1}{m} \sum_{j=1}^m \left( \frac{1}{n} \sum_{k=1}^n x_{jk} \right) \right) \right]^2} \left( \frac{1}{nm} \sum_{j=1}^m \sum_{k=1}^n x_{jk} \right)^{-1} = \frac{\sigma_{\bar{x}_j}}{\bar{x}} \quad (6)$$

We calculated MAV and IAV for  $H_{p1}$  and  $H_{pswell}$ . In order to properly account for their variability, the calculation of MAV and IAV for wind-seas and swells included the sea states where  $H_{psea}$  and  $H_{pswell} = 0$ .

### 3.4.4. Wave height time-series analysis

Time series of wave height were extracted and analyzed in terms of  $H_s$ ,  $H_{psea}$ ,  $H_{pswell}$  and contributions ( $H_{psea}c$ ,  $H_{pswell}c$ ) at six different sites along the coasts of New Zealand. The chosen locations of such analyses were three nearshore points along the west coast:  $nw$  (174.474°E, 37.738°S),  $w$  (169.830°E, 42.980°S) and  $sw$  (167.547°E, 46.428°S), and three nearshore locations along the east coast:  $ne$  (176.527°E, 37.442°S),  $e$  (177.210°E, 39.935°S) and  $se$  (171.42°E, 44.920°S). The analysis comprised of a comparison between seasonal

**Table 2**

Statistics of improvement in wave height accuracy (%). Columns display the statistics calculated for each metric, along each side of the grid. Rows show the metric over which the percentual improvement (and correspondent statistic) was calculated.

	West				North				East				South			
	mean	stdev	min	max	mean	stdev	min	max	mean	stdev	min	max	mean	stdev	min	max
NRMSE	7.1	1.3	5.3	9.6	8.8	2.4	5.2	14.9	10.2	3.7	4.4	17.3	7.6	1.6	5.2	10.7
MAE	6.9	1.7	4.4	9.9	8.1	3.2	3.0	15.2	11.4	4.6	4.2	20.3	7.6	1.8	4.9	13.9

and annual variability of wave heights as well as correlating monthly anomalies of each wave parameter with the SOI, SAM and DMI atmospheric indices.

### 3.4.5. Sector analysis

One would expect a spatially large wave system to be present in the same partition for all points this system extends through. However, due to the way the wave spectra is partitioned, the spatial distribution of a single partition tends to contain patches of different wave systems depending on the wave climate of the area. As an example, two separate swells traveling in opposite directions, both in partition  $p2$  (as  $p1$  is reserved for wind-sea waves) will have their partitions rearranged as they propagate towards each other: along every spatial point where both swells are intersecting, the swell with the larger wave height will continue to occupy  $p2$  while the other swell system will be relocated to  $p3$ .

Hence, in order to provide a more uniform spatial analysis of the wave systems present along the New Zealand area, the wave parameters distributed along the partitions were rearranged into directional sectors according to where each wave system propagates from. The directional sectors comprise of 16 ( $s1$  to  $s16$ ) angular intervals of 22.5 degrees, matching the directions of a wind rose:  $348.75^\circ \leq s1(N) < 11.25^\circ$ ,  $11.25^\circ \leq s2(NNE) < 33.75^\circ$ , ...,  $326.25^\circ \leq s16(NNW) < 348.75^\circ$ . Thus, partitioned wave characteristics such as wave height and period ( $H_{pn}$ ,  $T_{pn}$ ) of swells propagating from directions ( $\theta_{pn}$ ) that match sector  $s1$  will be allocated in  $H_{s1}$  and  $T_{s1}$  respectively. The same will occur for the remaining swell systems that match their corresponding sectors. If more than one swell approach from the same directional sector, the value assigned to this sector will be the aggregated wave height of both swells. The sectorization procedure was also performed for the wind-sea partition, so that both wave systems could be analyzed separately. Statistics of mean and mean contributions were also computed for the wind-sea and swell sectors, for both normal and extreme conditions.

## 4. Results

### 4.1. Boundary correction

The statistics over the improvements obtained in wave height accuracy are shown in Table 2. The largest values in mean  $H_s$  improvement (10.2% and 11.4% for NRMSE and MAE) were found along the east coast points, which also presented the largest maxima (17.3% and 20.3%) and standard deviation (3.7% and 4.6%) for NRMSE and MAE. The west coast points presented the lowest values of mean (7.1% and 6.9%) maxima (9.6% and 9.9%) and standard deviation (1.3% and 1.7%), for the same metrics. In general, the grid sides more exposed to the westerly winds (west and south) were the less benefited by the correction, as opposed to the grid sides that are partially sheltered by the New Zealand landmasses.

### 4.2. Validation

The plots shown in Fig. 2 display the evaluation of three locations exposed to different wave climates around New Zealand. The Maunganui Bluff station (northwest of North Island) is mostly exposed to waves from the southwest quadrant, generated in the Southern/Indian

Oceans and the Tasman Sea (Gorman et al., 2003b; Rueda et al., 2019). At this location, the model presents RMSE values of 0.18 m, 1.5 s and  $12.4^\circ$  for  $H_s$ ,  $T_{m02}$  and  $\theta_m$  respectively. The normalized RMSE for  $H_s$  is 0.08 and for  $T_{m02}$  is 0.2. Low and positive bias values were found at this location: 0.18 m, 0.8 s for  $H_s$ ,  $T_{m02}$ , while a negative bias ( $-0.81^\circ$ ) was found for  $\theta_m$ . High correlation values of 0.9, 0.8 and 0.7 were found for the same parameters. Mokohinau Islands station, located on the northeast coast of the North Island, is reached by waves traveling from the North and South Pacific oceans. The land sheltering effects restrict the incoming wave direction from NW to ESE, NE to E being the dominant wave directions. The station records however show waves from all directions (second row of Fig. 2). Since the buoy is located 50 km from the coast, it allows enough fetch for the dominant winds (southwest along with northeasterlies) to generate these waves (Gorman et al., 2003b). Model comparison with buoy records shows RMSE values of 0.15 m, 0.66 s and  $37^\circ$  for  $H_s$ ,  $T_{m02}$  and  $\theta_m$ . The normalized RMSE was approximately 0.1 for both  $H_s$  and  $T_{m02}$ , biases of 0.19 m, 0.23 s and  $22^\circ$  for  $H_s$ ,  $T_{m02}$  and  $\theta_m$ . Finally, similar values of correlation compared to the previous site for  $H_s$ ,  $T_{m02}$  and wave mean direction (0.9, 0.81 and 0.74) were found. Our last set of plots display the comparison between model and buoy for the Banks Peninsula site, on the east coast of the South Island. The predominant waves at this location are generated in the Southern Ocean, arriving from the south-southwest (Gorman et al., 2003b). However as for the Mokohinau Islands station, the directional buoy records show a wider range of wave directions (Fig. 2, third row), mostly limited by the peninsula (and New Zealand) landmasses. Wave height comparison provided RMSE values of 0.14 m, NRMSE of 0.08, bias of 0.05 m and correlation of 0.88. For  $T_{m02}$ , the values of RMSE, NRMSE, bias and correlation were 0.89 s, 0.14, 0.09 s and 0.73 whilst the direction variable presented values of  $42.6^\circ$  of RMSE,  $-15^\circ$  of bias and a correlation of 0.73.

Validation results for the remaining buoy deployments are shown in Table 3. The hindcast validation along the northeast coast of New Zealand was performed against the Mokohinau, Mangawhai, Katikati and Pukehina buoys. For  $H_s$ , values of RMSE ranged from 0.09 m at Pukehina to 0.15 m at Mokohinau Islands, maximum and minimum values of NRMSE were 0.17 at Mangawhai and 0.09 at Pukehina. The lowest correlation (0.83) and largest bias (0.25 m) were found along Katikati and Mangawhai while Pukehina presented the highest correlation (0.91) and lowest bias (0.1 m). Second order period RMSE varied from 0.66 s (Mokohinau Islands) to 2.13 s (Mangawhai). Normalized RMSE ranged from 0.13 at Mokohinau to 0.38 at Mangawhai. Negative bias values were found at the Mangawhai and Katikati stations,  $-0.7$  s and  $-0.2$  s respectively, being these the highest and lowest absolute values of bias found for the northeast stations. Correlation values estimated were the highest at Pukehina and Mokohinau (0.81) and the lowest at Mangawhai (0.6). In terms of direction, Pukehina and Mokohinau stations were validated against mean wave direction, which resulted in values of RMSE, bias and  $r$  of  $23.5^\circ$ ,  $-0.87^\circ$  and 0.86 for Pukehina and  $37.37^\circ$ ,  $22.19^\circ$  and 0.74 for Mokohinau Islands. Directional validation was performed with peak direction ( $\theta_p$ ) for Katikati and Mangawhai due to the characteristics of the equipment. The values of RMSE, bias and correlation found in these locations were of  $55.45^\circ$ ,  $-2.83^\circ$  and 0.37 for Katikati while for Mangawhai they were  $49^\circ$ ,  $0.97^\circ$  and 0.45.

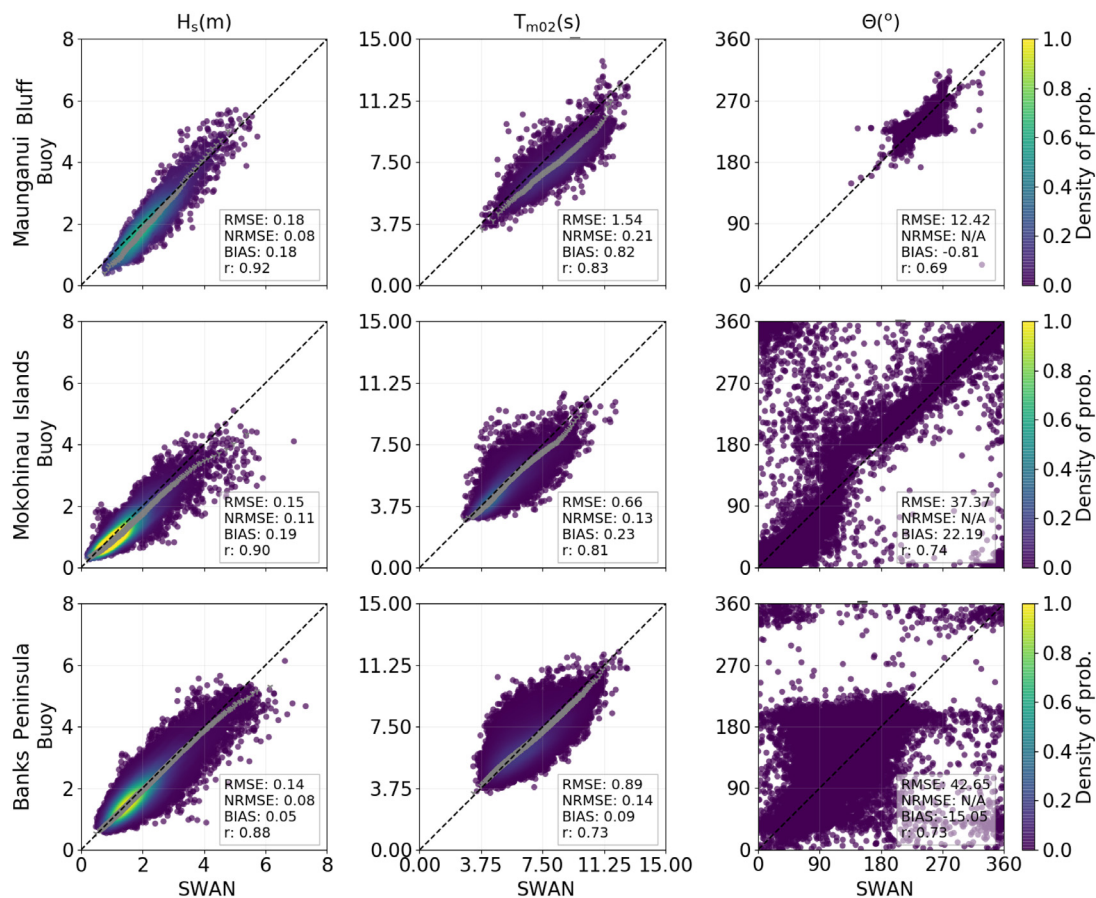


Fig. 2. Validation plots for three buoy deployments exposed to different wave climates around New Zealand. Rows display each location, columns show the tested wave hindcast parameters, scatter color represents the density of probability of occurrence and quantile distributions are shown in gray. Buoy measurements are plotted on the vertical axis while model estimations are plotted along the horizontal axis.

Table 3

Validation metrics for buoy and model. Rows show results for each location, columns display site name, depth as represented in the model and validation metrics for  $H_s$ ,  $T_{m02}$  and  $\theta$ . Deployments where the only directional parameter available is  $\theta_p$  are indicated by ‘+’, deployments with no directional parameters had their directional metrics filled with ‘-’.

Deployment site	Grid depth (m)	$H_s$				$T_{m02}$				$\theta$		
		rmse (m)	nrmse	bias (m)	$r$	rmse (s)	nrmse	bias (s)	$r$	rmse (°)	bias (°)	$r$
Maunganui Bluff	43.6	0.18	0.08	0.18	0.92	1.54	0.21	0.82	0.83	12.42	-0.81	0.69
Taharoa	26.7	0.20	0.10	0.08	0.87	2.42	0.35	1.03	0.73	-	-	-
Mokohinau I.	111.7	0.15	0.11	0.19	0.90	0.66	0.13	0.23	0.81	37.37	22.19	0.74
Mangawhai†	37.1	0.13	0.17	0.25	0.90	2.13	0.38	-0.74	0.60	49.17	0.97	0.45
Katikati†	32.8	0.12	0.15	0.15	0.83	1.21	0.24	-0.20	0.74	55.45	-2.83	0.37
Pukehina	65.7	0.09	0.09	0.10	0.91	0.76	0.16	0.30	0.81	23.50	-0.87	0.86
Baring Head	43.1	0.16	0.12	-0.09	0.87	1.36	0.23	-0.31	0.78	-	-	-
Golden Bay	30.4	0.05	0.08	-0.09	0.81	0.21	0.06	0.03	0.59	-	-	-
Banks Peninsula	79.7	0.14	0.08	0.05	0.88	0.89	0.14	0.09	0.73	42.65	-15.05	0.73

†Directional validation performed over peak direction due to equipment characteristics.

In general, off the west coast of New Zealand (Maunganui Bluff and Taharoa buoys) values of  $H_s$  are overpredicted by the model, with a bias of 0.18 m and 0.08 m for the Maunganui Bluff, and Taharoa stations respectively. The RMSE found in this area ranged from 0.18 m to 0.20 m, normalized RMSE and correlation values ranged from 0.08 to 0.10 and from 0.87 to 0.92, respectively. The second moment mean period was also overpredicted by the model (RMSE, NRMSE bias and correlation at Maunganui Bluff were of 1.54 s, 0.21, 0.82 s and 0.83). The Taharoa station presented values of 2.42 s, 0.35, 1.03 s and 0.73 for the same statistics. Finally, for  $\theta_m$ , the Maunganui Bluff deployment shows 12.42° of RMSE, -0.81° of bias and 0.69 of correlation.

A pair of buoys was used to evaluate the model in the Cook Strait area (the strait between the North and South Islands of New

Zealand). The Golden Bay station is located in the western portion of the strait (north coast of the South Island) and the Baring Head station is positioned towards the eastern end of the strait (southern coast of the North Island). While the Golden Bay buoy is sheltered from waves by Farewell Spit (a large sand spit on the northwest edge of the South Island) and the South Island’s landmasses, the Baring Head station is mostly exposed to southern swells. Validation showed good skill of the model in representing the wave climate of this area. Metrics for wave height obtained at each station were 0.16 m and 0.05 m of RMSE, 0.12 and 0.08 of normalized RMSE and a correlation of 0.87 and 0.81 for Baring Head and Golden Bay respectively. Both stations presented a negative bias of 0.09 m. The same metrics computed for  $T_{m02}$  presented values of approximately 1.36 s, 0.23, -0.31 s and 0.78 (RMSE, NRMSE, bias and  $r$ ) for Baring Head. Despite the better values of RMSE, NRMSE



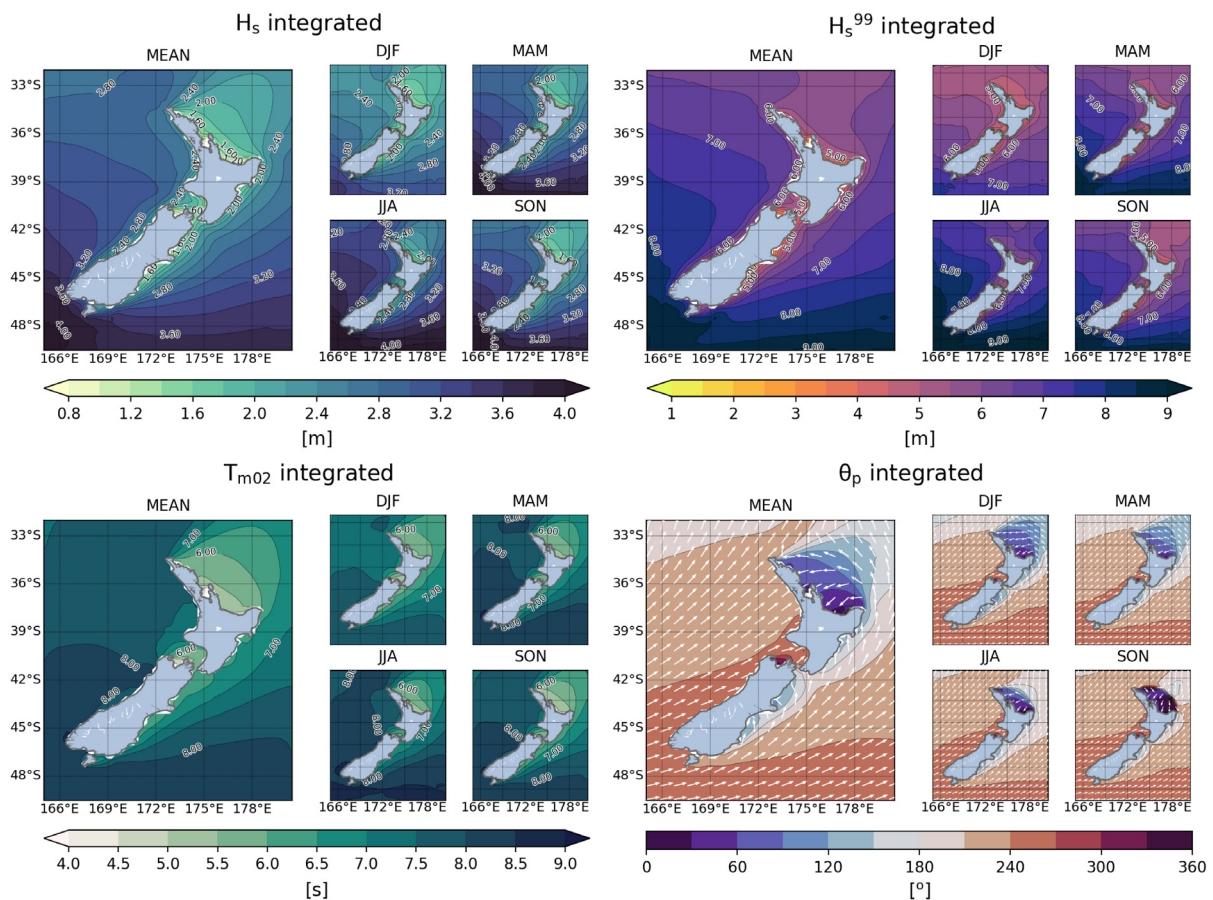


Fig. 3. Long term and seasonal averages of significant wave height (top left plot), extreme wave height (top right plot), second order period (bottom left) and peak direction (bottom right plot). The four smaller plots to the right of each large plot display the seasonal variability of the parameter shown, where DJF, MAM JJA and SON represent austral summer, autumn, winter and spring respectively. Values of each parameter plotted are represented by the respective colorbar. For wave direction, arrows point to the direction waves are traveling to and colors indicate the direction waves are traveling from.

and bias (0.2 s, 0.06 and  $-0.03$  s) found for Golden Bay, the station had a lower correlation value (0.59) than Baring Head.

The validation metrics were also calculated for the 9 km and 3 km grids. In general, the accuracy of the model improves as the resolution increases, nevertheless no site had its validation improved by higher resolution for all the estimated parameters.

### 4.3. Spatial distribution of integrated parameters

The mean  $H_s$  along the 20 years of hindcast data (top left of Fig. 3) shows nearshore wave heights of 3.4 m by the southwest of the South Island, progressively decreasing northeastwards, down to  $\sim 2.2$  m. Throughout the east coast of both islands, mostly sheltered from the southwesterly waves, the wave height varies around 1.9 m for the most exposed coasts and 1.6 m for sheltered coasts. The northeast coast of the country is not exposed to the prevailing southwesterly waves off the west coast, hence the predominant wave height of this area is between 1.6 m and 1.0 m. During the austral summer, while the wave height along the northeast coast is nearly the same, it decreases in about 0.4 m off the west and east coasts. Winter months present the largest average in wave height, with values increasing around 0.4 m throughout the country. Very similar wave height patterns occur during the autumn and spring months, however a slight clockwise rotation on the wave height bands is observed during spring (compared to autumn). No changes can be noted between the spring months and mean along the northeast coast of the North Island.

Along the south coast, mean values of  $H_s^{99}$  observed (top right of Fig. 3) range from 8 to 7.5 m, decreasing in height until  $\sim 6$  m northwards of the western shore. The northeast coast  $H_s^{99}$  mean is about 5 m along the most exposed shores, dropping to 4 m around the retreated beaches. Values from 5 to 3 m are present along the eastern shores. The seasonal variability observed for these events during MAM and SON is similar to the mean values, with a slight counter-clockwise rotation of the wave height bands during MAM, which increases the wave heights along the east coast and decreases along the west coast during these months. The total wave height change between the two seasons is approximately 0.5 m. During winter, wave heights increase by 0.5 m around the whole country, while in summer, a decrease of 1.5 m (west), 1 m (east) and 0.5 m (northeast) occur.

Mean values of  $T_{m02}$  (lower left, Fig. 3) vary between  $\sim 8.5$  s and 7 s throughout the west coast, 6 s to 5 s along the northeast coast and 6.5 s to 6 s on the southeast coast. During summer months,  $T_{m02}$  values reduce by 0.5 s along the west and southwest coasts and by  $\sim 0.4$  s along the northeast coast. Values observed during winter are increased by 0.5 s along the west and southeast coasts, with no significant change through the northeast coast. Autumn and spring values differ from the mean only across the northeast coast, with a slight increase (decrease) in  $T_{m02}$  during autumn (spring) along this location.

Mean and seasonal variability of  $\theta_p$  is displayed on the bottom right plot of Fig. 3. The mean direction along the west and south coasts is about  $240^\circ$ . Through the southeast, the direction arrows point northeastwards throughout the coast and northwards approaching the shore, while waves from  $\sim 30^\circ$  to  $90^\circ$  reach the northeast coast. The

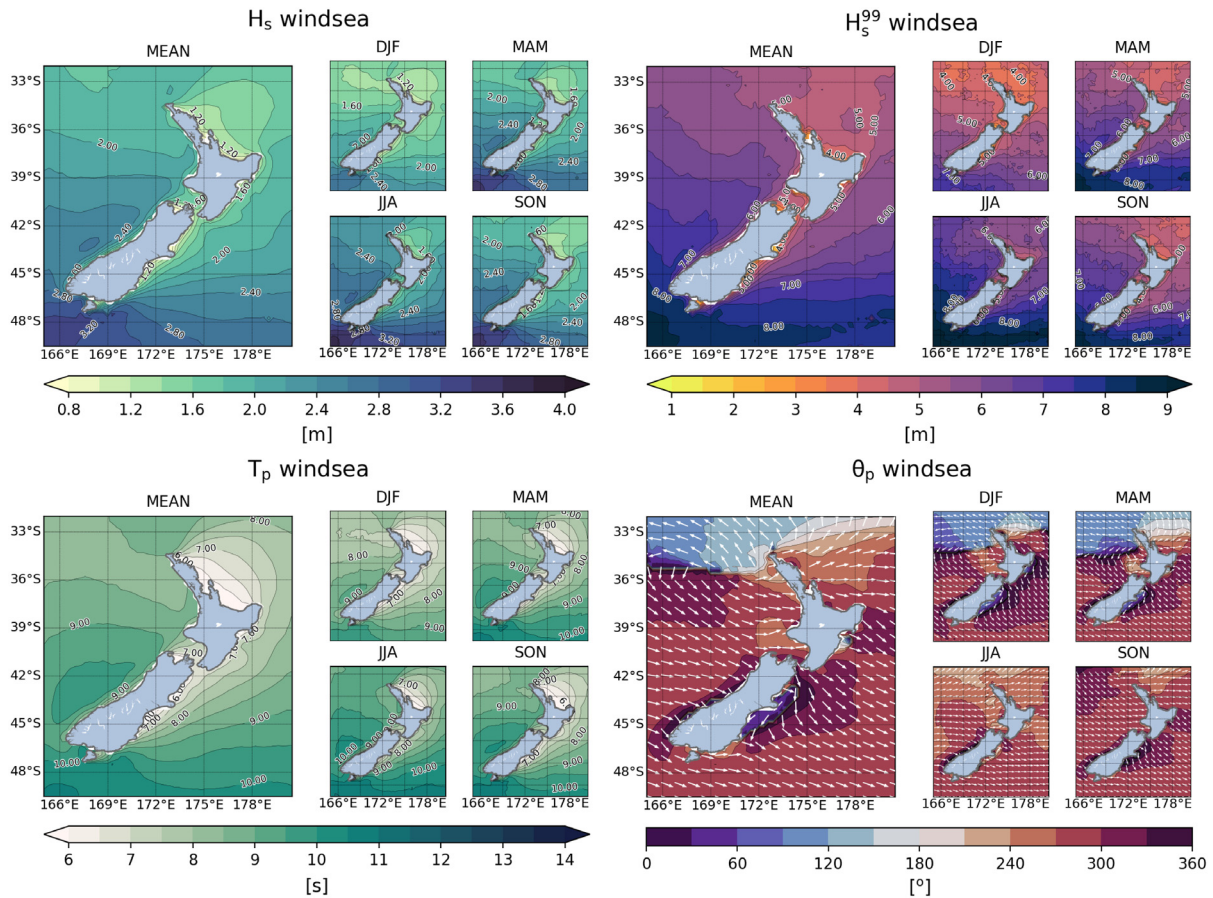


Fig. 4. Same as Fig. 3 but for wind waves. The period parameter shown in the bottom left plot is the peak period.

seasonal averages show a stronger southerly component during summer and autumn for the west coast and a stronger southwesterly component along the southeast coast during spring. The northeast coast shows a progression from easterly to north–northeasterly on autumn, winter and spring, returning to a more easterly peak direction during summer.

#### 4.4. Spatial distribution of partitioned parameters

The same statistics presented in the previous subsection as well as the  $\alpha$  for wave heights were calculated for the wind-sea (Fig. 4) and swell (Fig. 5) partitions over the 20 years of data. The mean values of wind-sea wave heights,  $H_{p1}$ , (top left of Fig. 4) range from 2.8 to 1.6 m along the west coast, with lower values along the southeast (~2.4 to 1.4 m) and northeast (~1.4 to 0.8 m) coasts. Seasonal values during autumn and spring months are slightly higher than the mean with similar spatial patterns. Winter months show values approximately 0.3 m higher while summer values are ~0.4 m lower than the mean. Values of the mean  $H_{p1}$  contribution (left plot of figure 1 of supplementary material), expressed in terms of  $\alpha$ , ( $\alpha_{sea}$ ) increase southwards and northwards of New Zealand, as well as through the Cook Strait. The areas off the west and east of New Zealand show values from 20 to 28%. Seasonal variability of the same parameter shows similar patterns, with an increase in the windsea presence during spring and winter.

Statistics of mean wind-sea wave height during  $H_s^{99}$  events (top right, Fig. 4) show values ranging from 8 to 6.5 m from south to north of the west coast, 8 to 4.5 m along the southeast coast (4 m in sheltered areas) and ~5.5 m to ~3 m through the northeast coast. Seasonality shows similar values during autumn and spring, an increase of about 0.5 m throughout the country during winter, and a reduction of ~0.5 (west) to 1 m (east and northeast) on summer. The  $\alpha$  of wind-sea waves during such events (left plot, supplementary figure 2) ranges from 85%

for the southwest of New Zealand, progressively decreasing to 60% northwards. Along the southeast coasts, values range from 95% to 75% whilst the northeast shows mostly values around 65%.

Mean values of  $T_{p1}$  (bottom left of Fig. 4) show larger values along the west coast (10 to 8 s) compared to the east (9 to 6 s) and northeast (~6 s) coasts. During summer months, this parameter decreases in ~0.5 along the southern coasts. Autumn and spring months' values are similar to the mean, while winter values are about 0.5 s higher than the mean throughout the west and southeast coasts.

Wind-sea waves peak direction (Fig. 4, bottom right) shows most of the country surrounded by waves from the NW quadrant. This directional pattern changes to NE along the east coast of the South Island and to SE northwestwards of the North Island. Similar patterns are present on summer and autumn months, except for a stronger easterly component round 38°S on these seasons. A dominant westerly component is observed on winter and spring, the first showing a SW dominance along the North Island, the latter with predominant NW and W wave systems throughout both islands.

The spatial distribution of  $H_{pswell}$  waves (top right plot of Fig. 5) is similar to the wind-sea waves'.  $H_{pswell}$  values however have weaker longshore gradients, and stronger cross-shore gradients, decreasing shoreward from ~2.8 m to approximately 2 m along the west coast, and from 2.6 m to 1.4 m along the southeast coast. The northwest area shows values between 1.2 m and 1.0 m. Seasonality displays similar values during autumn and spring months and a 0.2 to 0.4 m change, negative during summer and positive during winter. Mean values of swell's  $\alpha$  ( $\alpha_{swell}$ , supplementary figure 1, right) show the opposed patterns found in  $\alpha_{sea}$ , as per definition ( $\alpha_{sea} + \alpha_{swell} = 1$ , supplementary figure 1, left).

Extreme height of swells (Fig. 5, top right) shows larger mean values of  $H_{pswell}$  off the west coast (4 m to 5 m), with the largest values



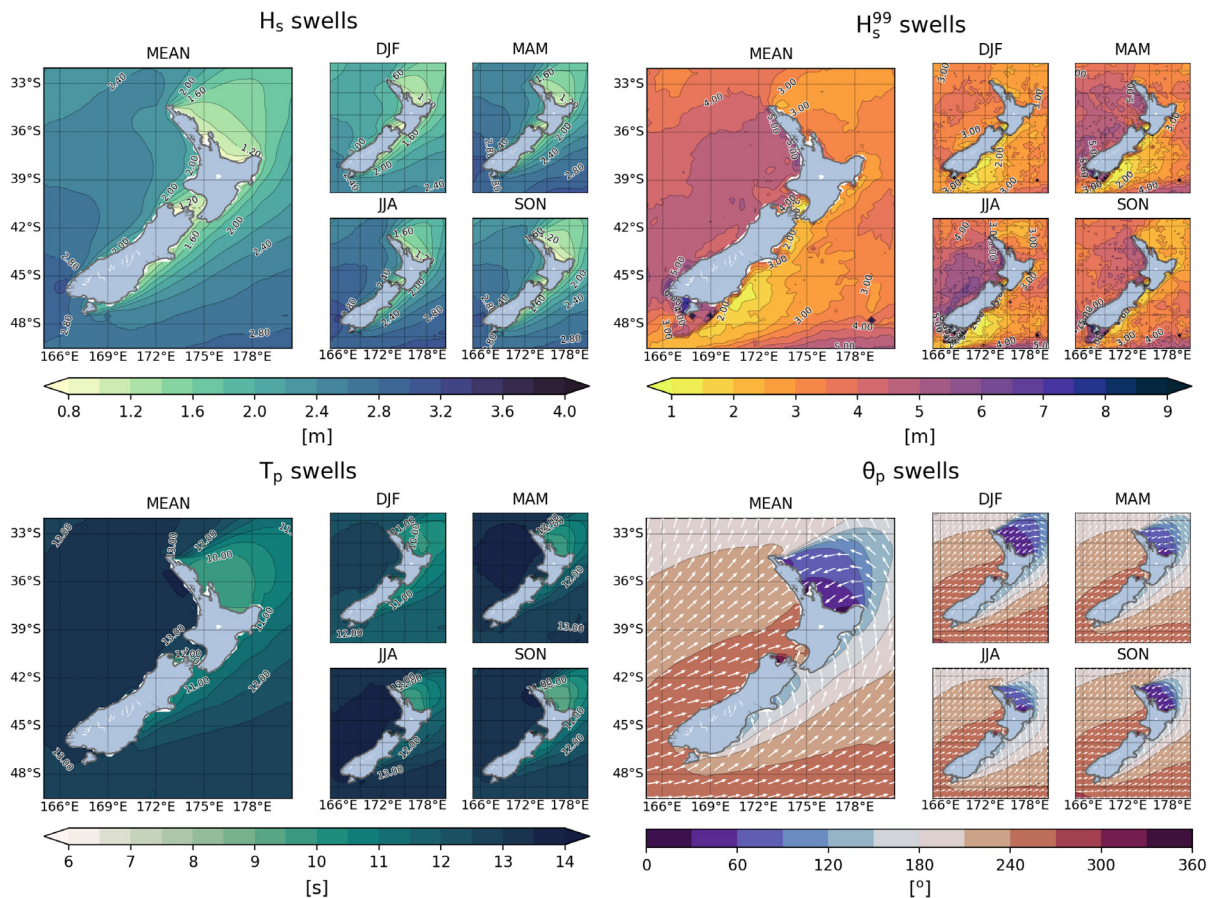


Fig. 5. Same as Fig. 4 but for aggregated swells.

along the northwest coast (~5 m) and between the South Island and Stewart Island (small island near the southern edge of the country, values ranging between 4 m and 6 m). Values of  $H_{pswell}$  vary from ~3 m (south) to ~3.5 m (north) along the east coasts. Seasonality shows similar patterns of wave heights, with larger variability off the west coast — the lowest wave heights occur during summer (~1.5 m lower than the mean off the west), progressively increasing on spring (~0.5 m lower), winter and autumn (both slightly larger than the mean). The  $\alpha_{swell}$  values (right of figure 2, supplementary material) are the complement of the  $\alpha_{sea}$  values (left plot of figure 2, supplementary material).

The 20-year mean of peak period of the aggregated swell partition ranges from 13 s to 10 s (Fig. 5, bottom left). The lowest values are found in the northeast coast (~10 s) while values of approximately 13 s are observed through the west coast, and values of ~11 s are present along most of the southeast coast. The mean patterns are similar to spring, and a general increase of 0.5 s occurs during autumn and winter, with a decrease (0.5 s) during summer.

Spatial patterns of peak swell direction are very similar to the peak wave direction (bottom right of Figs. 3 and 5 respectively). Noticeable differences are a stronger westerly component through the west coast (shifting northwards the 240° band between 42°S and 38°S), and an eastward (north-eastward) deviation of the directional bands through the southeast (northeast) coast. The seasonal variability of  $\theta_p$  for swells is similar to the integrated  $\theta_p$  changes, again with the swells displaying stronger westerly/southerly directional components.

The exposure of New Zealand to a number of wave generation basins results in many areas where crossing, opposing or following swells occur, as per Fig. 6. The average incidence of crossing seas (first column, Fig. 6, top) indicates their presence along the less sheltered areas of the country: south and eastward of the South Island (40% to

35%), eastwards of the East Cape (eastern end of the North Island, values around 30%) and northwestwards of Cape Reinga (northernmost point of the North Island, values within 25%). Another area with values around 30% is observed northwestwards of the Cook Strait while the remaining areas around the country present values between 15% and 5%. Seasonality (not shown) in general shows similar spatial patterns, with an overall decrease of 5 percentage points (%p) in summer, an increase of 5%p southwest (and a decrease of 5%p northwest) of the country during spring, a 5 to 10%p increase northwards of 41°S in winter and a 5%p reduction west (10%p increase northwestwards) of New Zealand in autumn.

The distribution of crossing seas change considerably during events of extreme wave heights (Fig. 6, bottom left) as the highest occurrences are found northwards and the lowest are found southwards. Mean values show a 15% area along the south of South Island and a 10% to 30% area through the west and southeast coasts. The highest values are around 35% off the northeast coast and eastwards of East Cape (up to 50%). Seasonal plots (not shown) indicate high incidence of crossing seas along the south of South Island, westwards of the Cook Strait, northwards and northwestwards of the northeast coast during summer. Autumn and winter values are similar to the mean, with higher occurrence of crossing seas along and eastwards of the northeast coast, while in spring the higher occurrence of such seas is eastwards of the Cook Strait and the East Cape.

Opposing swells are more likely to occur near the northwest and southeast extremes of New Zealand’s landmasses (second column of Fig. 6, top). Mean values show a band of 15% of occurrence crossing part of the study area, starting around 36°S and stretching north-eastwards towards Cape Reinga. Another area is observed along the southeastern coast of the South Island, extending southwestwards and northeastwards of this coast, with values from 30% to 15%. Seasonality

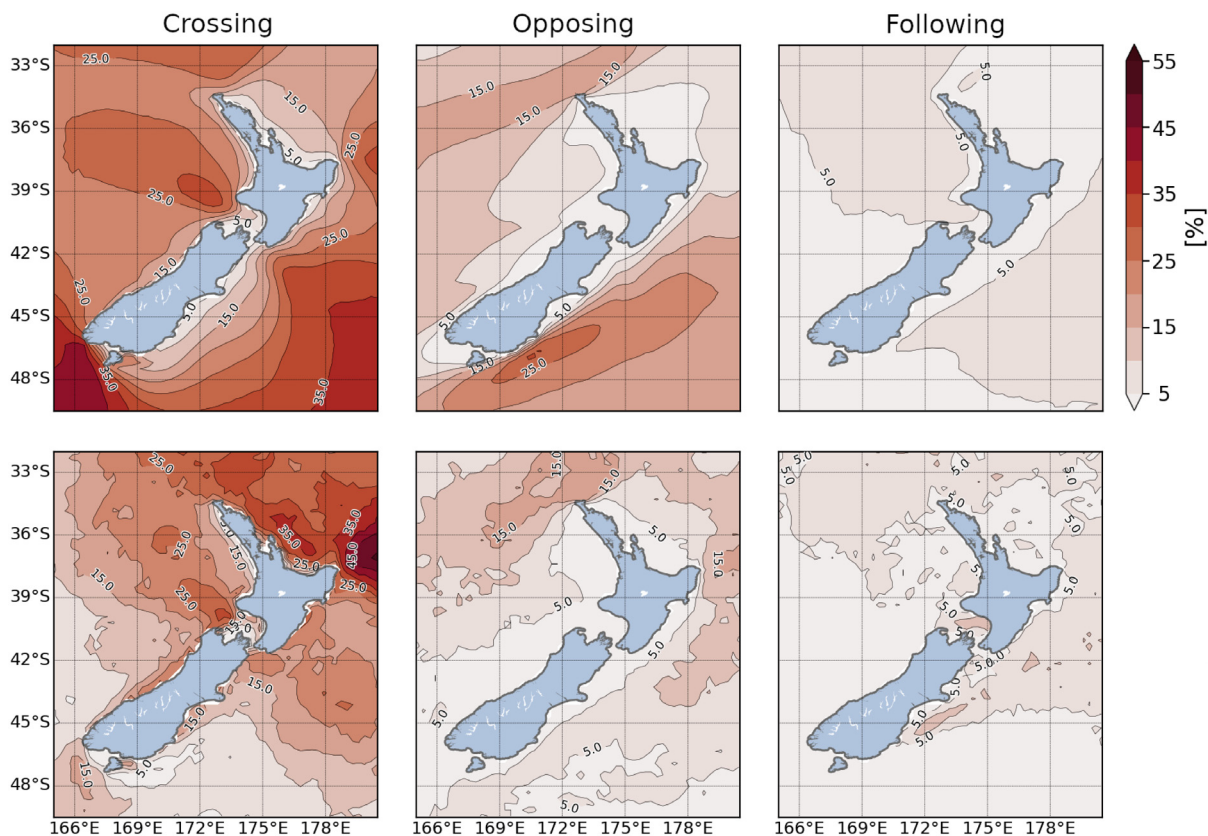


Fig. 6. Mean occurrence of crossing ( $90^\circ \pm 30^\circ$ ), opposing ( $180^\circ \pm 30^\circ$ ) and following ( $0^\circ \pm 30^\circ$ ) seas with wave heights higher than 1 m (top) and during events of extreme wave heights (bottom). Colors in plots correspond to values shown in colorbar.

(not shown) displays similar patterns in summer (with a narrower 20% band northwestwards of Cape Reinga) and spring (with a shift northeastwards of the 15% band near Cape Reinga), an overall increase of 5%p along the areas of opposing seas in autumn, and a widening in the 15% band to the west (and the 25 and 20% bands southeast) of the country in winter.

Patterns of opposing seas also change significantly during storm events, as per Fig. 6 (second column, bottom). The highest values (~15%) are observed near the northern extremes of the country (Cape Reinga and East Cape), decreasing southwards towards the west and southeast coasts. The highest seasonal values (not shown) are observed eastwards of Cape Reinga in summer and autumn, east/westwards of the northeast coast and south of South Island in winter, and north of Cape Reinga/east of the southeast coast during spring.

Following swells (Fig. 6 top left) occur at a rate lower than 5% for all nearshore waters throughout New Zealand, with a 5% band close to the west coast of the North Island and east of the southeast coast of the country. Seasonality (not shown) displays this band shifting offshore in summer, onshore in winter (with the appearance of a 10% area northwestwards of Cape Reinga) and no significant changes during autumn and spring months.

During extreme events, both areas of over 5% occurrence of following seas shift northwestwards and a few areas of 10% occurrence appear inside Cook Strait and east of the South Island. The highest values of such seas occur in autumn (up to 15%), with a spatial distribution similar to the mean. Small changes in the spatial distribution of following seas occur during the remaining seasons (not shown).

#### 4.5. Annual variability and time series of integral and partitioned parameters

Integrated  $H_s$  MAV values (Fig. 7, top left) range around 40% throughout most of the west and east coasts, also showing slightly larger values in sheltered areas along the northeast coast and Cook Strait. Mean annual variability of wind-sea waves are the largest (Fig. 7, top center) varying from ~132% to ~156% along the west and southeast coasts, with larger values on the nearshore areas. Smaller MAV values are present southwest of the South Island (~114%), at each end of Cook Strait (~102%) and through the northeast coast (96%). The MAV values of swell waves are approximately 6 to 12%p larger than of integrated parameters (Fig. 7, top right), showing the largest values along the south of South Island (~60%), the Cook Strait (~70%) and the northeast coast (~70%).

The  $H_s$  IAV over the 20-year hindcast (bottom left of Fig. 7) display values around 4.5% along most of New Zealand coasts, with the highest variability of wave height inside the Cook Strait (between 6% and 7%). Wind-sea waves IAV (bottom center, Fig. 7) ranges around ~9% west and southeast of New Zealand, with lower values to the east and northeast of the country. Inter annual variability of swell waves (Fig. 7, bottom right) is larger along the western coasts (~5%), followed by the southeast (~4.5%) and northeast coasts (~4%).

#### 4.6. Wave height and climate indices

Time series of  $H_s$ ,  $H_{psea}$  and  $H_{pswell}$ , together with their seasonal and annual means for the three points along the west (nw, w and sw) and east (ne, e and se) coasts of New Zealand are shown in Figs. 8 and 9.

The time series of the west coast allow us to observe how the total wave height is mostly dominated by swell waves, with eventual sea



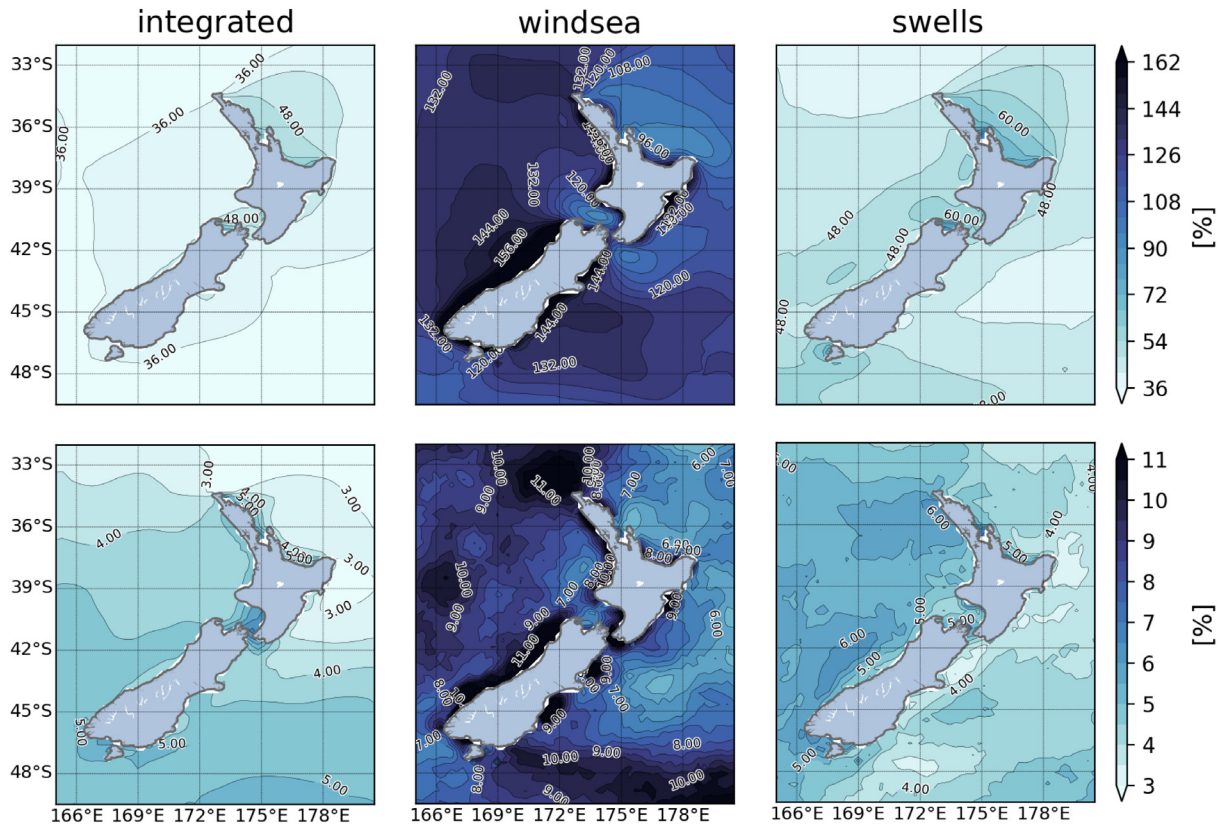


Fig. 7. Spatial patterns of mean annual variability (MAV, top) and inter annual variability (IAV, bottom). Columns show values for integrated parameters, wind-sea waves and swell waves. Values displayed on plots are identified by the colorbar on the right of each row.

Table 4

Correlation values at locations *nw* (174.474° E, 37.738° S), *w* (169.830° E, 42.980° S) and *sw* (167.547° E, 46.428° S). Rows display the different wave parameters correlated, columns show the locations and indexes used. Values in bold indicate statistically significant coefficients within the 95% confidence interval.

	nw			w			sw		
	SOI	DMI	SAM	SOI	DMI	SAM	SOI	DMI	SAM
$H_{psea}$	-0.13	0.13	-0.09	-0.01	<b>0.13</b>	-0.16	-0.11	<b>0.15</b>	-0.08
$H_{psea}^c$	-0.07	0.02	<b>-0.24</b>	0.02	0.07	<b>-0.22</b>	-0.09	0.08	<b>-0.31</b>
$H_{pswell}$	-0.12	<b>0.19</b>	-0.03	<b>-0.13</b>	<b>0.22</b>	-0.02	<b>-0.16</b>	<b>0.29</b>	<b>0.15</b>
$H_{pswell}^c$	-0.07	<b>0.15</b>	0.04	-0.11	<b>0.15</b>	0.05	<b>-0.16</b>	<b>0.28</b>	<b>0.21</b>
$H_s$	-0.13	<b>0.16</b>	-0.12	-0.10	<b>0.19</b>	-0.12	<b>-0.18</b>	<b>0.28</b>	0.07

states dominated by wind-sea waves. Seasonal mean values show the variability of the total, wind-sea, and swell wave heights, with eventual occasions (seasons) where the wind-sea mean wave height (i.e., mean of the wind-sea wave heights that are larger than 0 m) is larger than the total wave height. Points *nw* and *w* show similar mean values of  $H_{sswell}$ , meaning that the wind-sea waves are responsible for the difference in total wave height between the two sites. At location *sw* we can observe a reduction in the height of wind-sea waves and the predominance of swell waves for most of the time series. Mean swell wave height is larger at point *sw* whilst wind-sea wave height is slightly lower, compared to *nw* and *n*.

The annual mean plots show a more similar pattern in the total wave height oscillation between points *nw* and *w* than site *sw*. The first two locations present a sawtooth pattern along the years whilst the latter shows strong changes in some years followed by small oscillations in the next years. It is also possible to observe that the yearly swell wave height oscillation differs from that of the wind-sea for all sites. For the east coast, despite the swell wave predominance throughout the country, the time series of wave height at point *ne* (Fig. 9) shows more wind-sea dominated sea states compared to points *e* and *se*. The mean

annual values of wave height show a more similar behavior between sites *e* and *se* compared to *ne*.

Correlation between climate indices and wave heights at each western point (Table 4) shows low but statistically significant values for SOI and  $H_{psea}$  at location *nw* (-0.13). The SOI also presents robust correlation for  $H_{pswell}$  (-0.13) at site *w*, and for  $H_{pswell}$  (-0.16),  $H_{pswell}^c$  (-0.16) and  $H_s$  (0.18) for site *sw*. The DMI correlates with  $H_{pswell}$ ,  $H_{pswell}^c$  and  $H_s$  at all locations, and also with  $H_{psea}$  at points *w* and *sw*. The largest correlation values of the DMI are for swell wave heights (time series of  $H_{pswell}$  at *w* shown in Fig. 10, top), the highest at site *sw* (0.29). For wind-sea wave height, the correlation is of 0.13 and 0.15 at points *w* and *sw*. The SAM index correlates with  $H_{psea}^c$  at *nw* (-0.24) and with  $H_{psea}$  (-0.16) and  $H_{psea}^c$  (-0.22) at point *w* (time series for  $H_{psea}^c$  at point *w* shown in Fig. 10, bottom). The *sw* location shows positive correlation between SAM and  $H_{pswell}$  (0.15),  $H_{pswell}^c$  (0.21) and negative correlation for  $H_{psea}^c$  (-0.31).

For the east coast locations (Table 5), robust correlation was found for the SOI index only at point *e*, for  $H_{psea}^c$  (0.19). Correlation between wave parameters and the DMI index was found at point *se* with values of 0.14 for  $H_s$  and 0.15 for  $H_{psea}^c$ . The SAM index correlates with swell

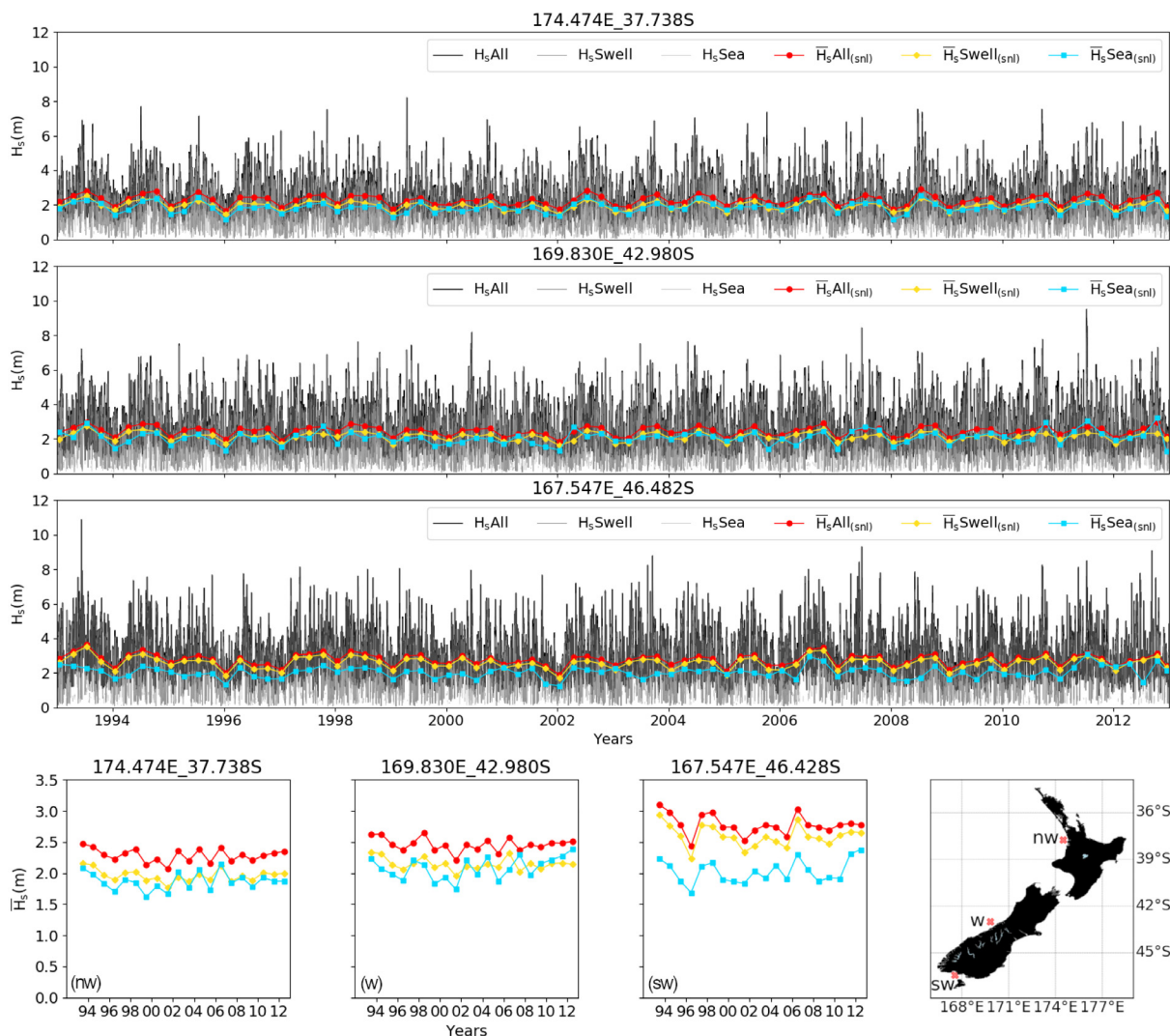


**Fig. 8.** Wave height timeseries of the three different locations along the west coast of New Zealand: points *nw* (174.474°E, 37.738°S, first row), *w* (169.830°E, 42.980°S, second row) and *sw* (167.547°E, 46.428°S, third row). Lines plotted in black, darkgrey and lightgrey show the 3-hourly total, wind-sea, and swell wave heights respectively. Red lines with circles, yellow lines with diamonds and light blue lines with squares show the seasonal (DJF, MAM, JJA, SON — first to third row plots) and yearly (fourth row, first to third columns) mean wave heights of integrated, swell and wind-sea waves. Geographic location of each point is shown in the bottom right map.

**Table 5**

Same as Table 4 but for points *ne* (176.527° E, 37.442° S), *e* (177.210° E, 39.935° S) and *se* (171.42° E, 44.920° S) along the east coast.

	ne			e			se		
	SOI	DMI	SAM	SOI	DMI	SAM	SOI	DMI	SAM
$H_{psea}$	0.10	-0.12	-0.04	0.09	-0.02	<b>0.19</b>	0.10	0.07	0.07
$H_{psea}^c$	0.02	-0.06	-0.12	<b>0.19</b>	0.01	0.02	0.13	<b>0.15</b>	-0.02
$H_{psewell}$	0.06	-0.10	<b>0.16</b>	-0.04	-0.03	<b>0.14</b>	-0.06	0.10	-0.00
$H_{psewell}^c$	0.05	-0.09	<b>0.16</b>	-0.05	-0.04	<b>0.15</b>	-0.06	0.09	0.00
$H_s$	0.07	-0.11	0.03	0.05	-0.02	<b>0.15</b>	0.02	<b>0.14</b>	-0.01

and swell contribution at site *ne*, and with all but  $H_{psea}^c$  parameters at point *e*, with the largest correlation for  $H_{psea}$  (0.19).

#### 4.7. Directional means of sectorized partitions

Wind-sea and swell mean wave heights of the 16 directional sectors are shown in Fig. 11 (top). A noticeable feature is the higher wave energy of the southwesterly (clockwise from SW to W) sectors (wind-sea and swells) over the other remaining directions and the high values still found in the SSW and W sectors. Wave heights of wind-sea and swells are remarkably larger for these sectors, with wind-seas ranging roughly

from 4 m southwest of the South Island, decreasing northeastwards (< 3 m) and showing their lowest values along the sheltered coasts of the North and South islands. Swell values for these sectors are also higher, with values ranging from 2.5 m to 2 m at the southwest corner of the study area, also decreasing northeastwards and showing lower values along the sheltered areas of both islands. The remaining plots of Fig. 11 (top) display values from ~2 m to ~1 m for wind-sea waves and from ~1 m to < 0.5 m for swell waves, with patterns changing according to the wave direction. The most noticeable features are the shadowing effects of New Zealand landmasses and the increased wave height near the western end of the Cook Strait for the southeastern swells and the

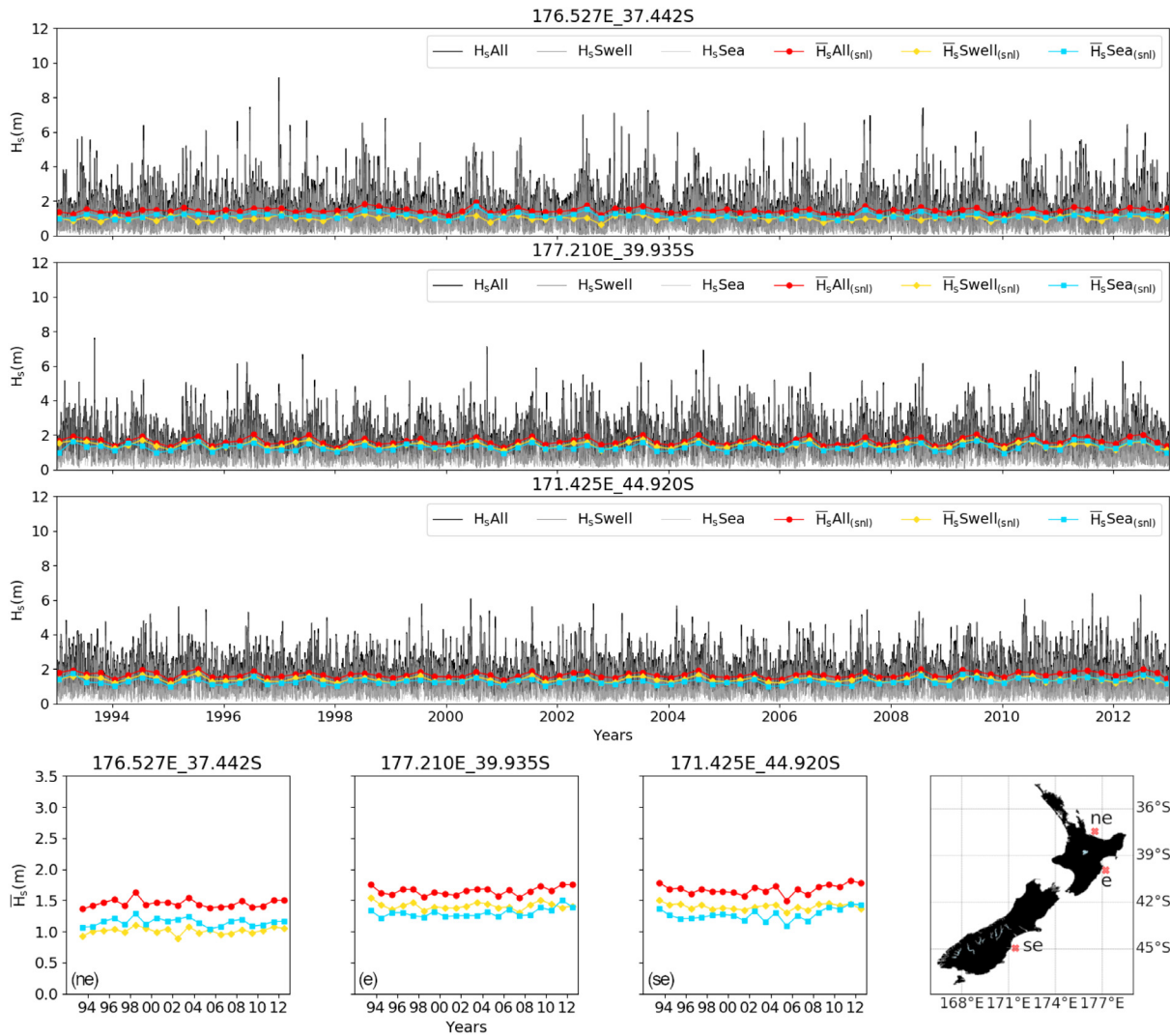


Fig. 9. Same as Fig. 8 but for three different locations off the east coast, as displayed in the bottom map. Points are: *ne* (176.527°E, 37.442°S), *e* (177.210°E, 39.935°S) and *se* (171.42°E, 44.920°S).

same increase in wave height for the opposite end of Cook Strait and northwestern wave systems.

The wave height contribution in terms of  $\alpha$  shown in Fig. 11 (bottom) allows us to observe the actual weight of each directional wave system all around New Zealand. In particular, how the swell contribution compares to the wind-seas', despite the latter present larger wave heights. These plots also indicate how representative are the wave systems from NNE to ESE (clockwise) along the northeast and east coasts, and the wave systems from SE to SSE (clockwise) throughout the southeast coast and northwards of the northeast coast. The wave systems from S to WSW show the highest contribution rate along the west and south east coasts, with the largest values for swells. The swell plots for these sectors also show in their gradients the amount of wave energy that propagates northwards (or eastwards) of the grid, and the amount that refracts towards the shore.

Fig. 12 (top) displays the mean wave height of directional sectors during  $H_s^{99}$  events. Once more, wind-sea waves are responsible for most of the energy during these events and the southwesterly sectors (clockwise from SSW to W) present the highest values of  $H_s^{99}$ . Wave heights observed in these sectors are within ~8.5 m (SW of the study area), gradually reducing to 5.5 m across the west coast and showing lower values at the sheltered areas/coasts. The remaining sectors mostly show values of sea wave height ranging approximately from 3.5 m (north of the study area) to 6.5 m (south of the study area) and swell waves

ranging from 0.5 m to 4.5 m, with different spatial distributions of wave heights for each sector. Noticeable patterns observed are the white areas indicating total wave absence along such area and sector, and the different shadowing effects of New Zealand landmasses over wind-sea and swell waves, the latter showing a more counter-intuitive spatial distribution represented by relatively large swell wave heights offshore of sheltered areas (as from sectors NNE to ESE, clockwise).

The  $\alpha$  of each sector during  $H_s^{99}$  events, as per bottom plot of Fig. 12, shows contribution patterns similar to the  $\alpha$  plots of Fig. 11, but with a larger contribution of wind-sea than swells. The noticeable patterns are the strength of the NE to SE wind-sea waves over the northeast shore of the study area, the strong  $\alpha$  values of the SSE to SSW sectors along the southeast coasts, and the largest alpha of the SSW to WSW sectors (clockwise) along the west coast.

The relationship between  $H_{psea}$  and  $H_{pswell}$  is different when sector extreme means are analyzed, as per figure 3 (top) of the supplementary material. Compared to the wave height plots in Fig. 12 (top), the mean wave height of wind-sea waves is similar to the swells' wave height for almost all sectors and areas, with slightly different spatial patterns. Exceptions are on sectors from NE to S, where swells are generally higher than wind-seas along the eastern coasts, and on sectors from S to W (clockwise), in which wind seas are larger than swells.

For  $\alpha$  values of sector extremes (supplementary figure 3, bottom), in general the wind-sea waves have larger  $\alpha$  than swells, except along



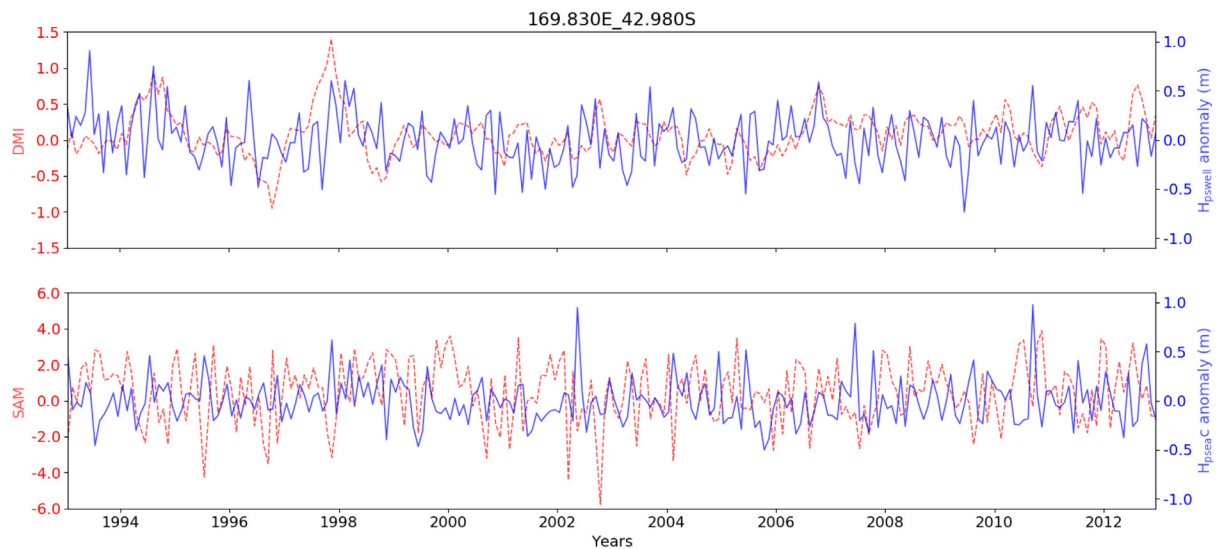


Fig. 10. Monthly anomalies of the DMI vs  $H_{pswell}$  (top) and SAM vs  $H_{pseac}$  (bottom) at location  $w$  (169.830°E, 42.980°S). Red dashed lines (scale at left vertical axis) show the atmospheric indices, blue solid lines (scale at right vertical axis) display the anomaly in wave height along the simulation years (horizontal axis).

the eastern coasts of New Zealand for sectors NE to S, where  $\alpha_{swell}$  is larger than  $\alpha_{sea}$ .

## 5. Discussion

The hindcast here presented contributes to the current knowledge base of the New Zealand wave climate by addressing a more recent time frame than Gorman et al. (2003b) and the hindcast studied in Godoi et al. (2016, 2017). In addition, it provides a more comprehensive set of wave parameters, in a higher resolution compared to the other databases. This data shall also benefit future studies that aim to exploit partitioned information from multimodal wave spectra.

The correction technique applied to the boundary points resulted in significant improvements in the wave height. The differences in the results between the north and east sides versus the west and south sides of our downscaling grid are related to the effect of New Zealand landmasses on winds and waves, together with the calibration method. Specifically, New Zealand's North and South Islands block the westerly winds and wave systems. As a result, errors can occur in the wave generation throughout the east and north coasts, as the winds along these areas are misrepresented due to the atmospheric models resolution and the complex orography (Cavaleri and Bertotti, 2004) of the North and South Islands. Apart from that, the correction method performs better for wind-sea dominated sea-states along the west coast (Albuquerque et al., 2018), which is mostly dominated by swells (figure 1 of supplementary material), while the swells correction performs better throughout the east coasts. Hence, whilst the west coast is slightly benefited from the correction of wind-seas, other multimodal sea states (present along the north and east sides of the grid, supplementary figure 1) benefit from the correction of each (of up to 6) wave system present.

The validation results showed good agreement between buoy and hindcast data around New Zealand. Roughly, the model estimates the wave heights with a positive bias of 0.08 m to 0.18 m along the west, 0.25 m to 0.1 m along the northeast and 0.05 m to  $-0.09$  m through the southeast coasts. Second moment period is overestimated along the west (0.8 s to 1.0 s) and over or underestimated off the northeast (0.3 s to  $-0.74$  s) and southeast coasts (0.03 s to  $-0.31$  s), depending on the validation site. The downscaling and validation were not performed for raw (non-corrected) wave boundaries due to the significant computational effort required. Such comparison should be addressed in a future study.

Four buoy moorings are available within the time-span of the present hindcasts and the one by Gorman et al. (2003b): Baring Head, Katikati, Mokohinau Islands and Mangawhai. Comparison<sup>1</sup> between the present validation results and the validation provided in Gorman et al. (2003b) along these locations shows lower scatter, slightly higher bias (0.08 m) and similar correlation for wave height. Second moment period comparison shows our database with slightly higher scatter, lower bias ( $-0.5$  s) and higher correlation. We were not able to compare both hindcasts in terms of wave direction as no directional validation is available in Gorman et al. (2003b). The hindcast studied by Godoi et al. (2016, 2017) had no extensive validation published, however, according to the authors, it presents an average RMSE of 0.5 m and a correlation of 0.83 for wave height, meaning that our hindcast performs slightly better.

Despite the higher accuracy of our model, errors and differences with measurements are somehow expected, as they are inherent to the wave modeling process. Along with the many elements that can affect these results (i.e., boundary forcings, grid resolution, model physics and numerical errors), wind forcings can be a significant factor, as they are the main driving force for ocean waves (Chawla et al., 2013). It should be observed therefore, that the wind database used in this study has a higher temporal and spatial resolution compared to the wind fields of the previous studies. Also, the bias of the wind database used in our 20-year simulation has changed along these years. Compared to the available altimeter data, CFSR wind speeds (90th, 95th and 99th percentiles) were overestimated, particularly in the Southern Hemisphere (Chawla et al., 2013). By mid 1993, the introduction of Special Sensor Microwave (SSM/I) ocean wind observations on CFSR noticeably decreased the existing bias. Later on, (2006) a small bias increase occurred, attributed to the inclusion of several satellite radiance data streams to the CFSR analysis (Chawla et al., 2013). In order to further understand these biases and how they can affect our hindcast, we used the method described in Albuquerque et al. (2018) to perform a directional comparison between satellite and CFSR wind speeds. Results (supplementary figure 4) indicate a general overestimation of the wind speeds offshore of New Zealand in all directions, except for some locations where an underestimation of the south and southwesterly winds was observed. Nearshore areas

<sup>1</sup> The difference between the average of each statistics along all sites for the present database and the same averages for table 2 (validation) in Gorman et al. (2003b).



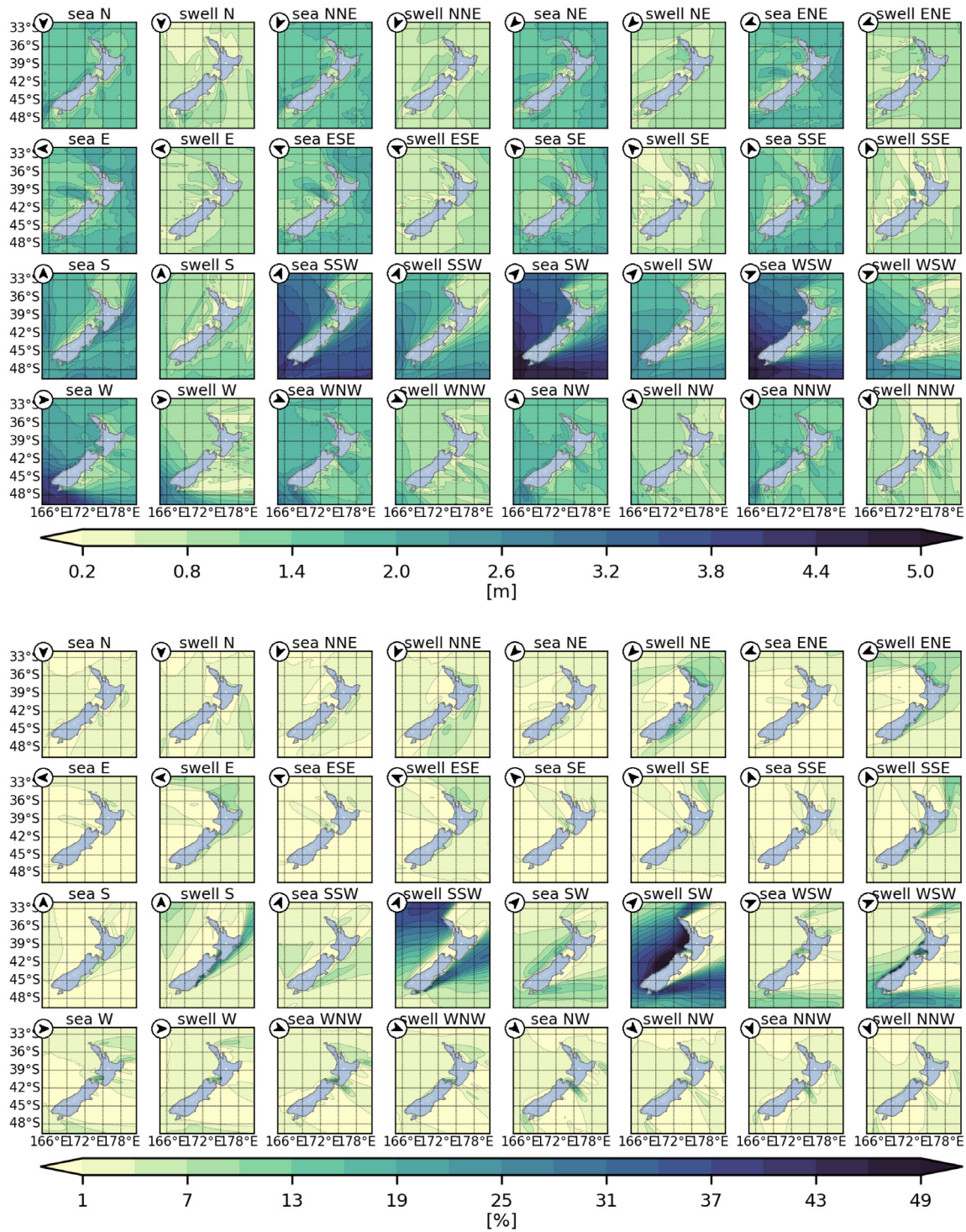


Fig. 11. Mean  $H_s$  of sea and swell waves from 16 directional sectors (top) and mean contribution of each sector in the aggregated wave height in terms of  $\alpha$ . Arrow on the top left of plots shows the direction waves travel to, plot titles indicate the wave type and direction waves comes from. Values for each parameter plotted are displayed by the plot's respective colorbar.

west of the South Island also presented underestimated wind speed values in the seaward directions. Such results suggest the possibility of a future study focussing on the changes in the hindcast's accuracy when downscaling with the corrected wind forcings.

The spatial analyses of integrated and partitioned parameters show how wind-sea and swell waves contribute to the mean value of the estimated parameters. The wave heights are mostly dominated by swell

waves in terms of mean values and wind-sea waves in terms of extreme values. The mean wind-sea waves are responsible for approximately 20% to 40% of the total nearshore wave height while the rest is complemented by swell waves (figure 1 of supplementary material). The increased presence of wind-seas along the study area is either related to the presence of strong winds (i.e., Cook Strait and south of South Island) or due to the sheltering effects of New Zealand (northeast



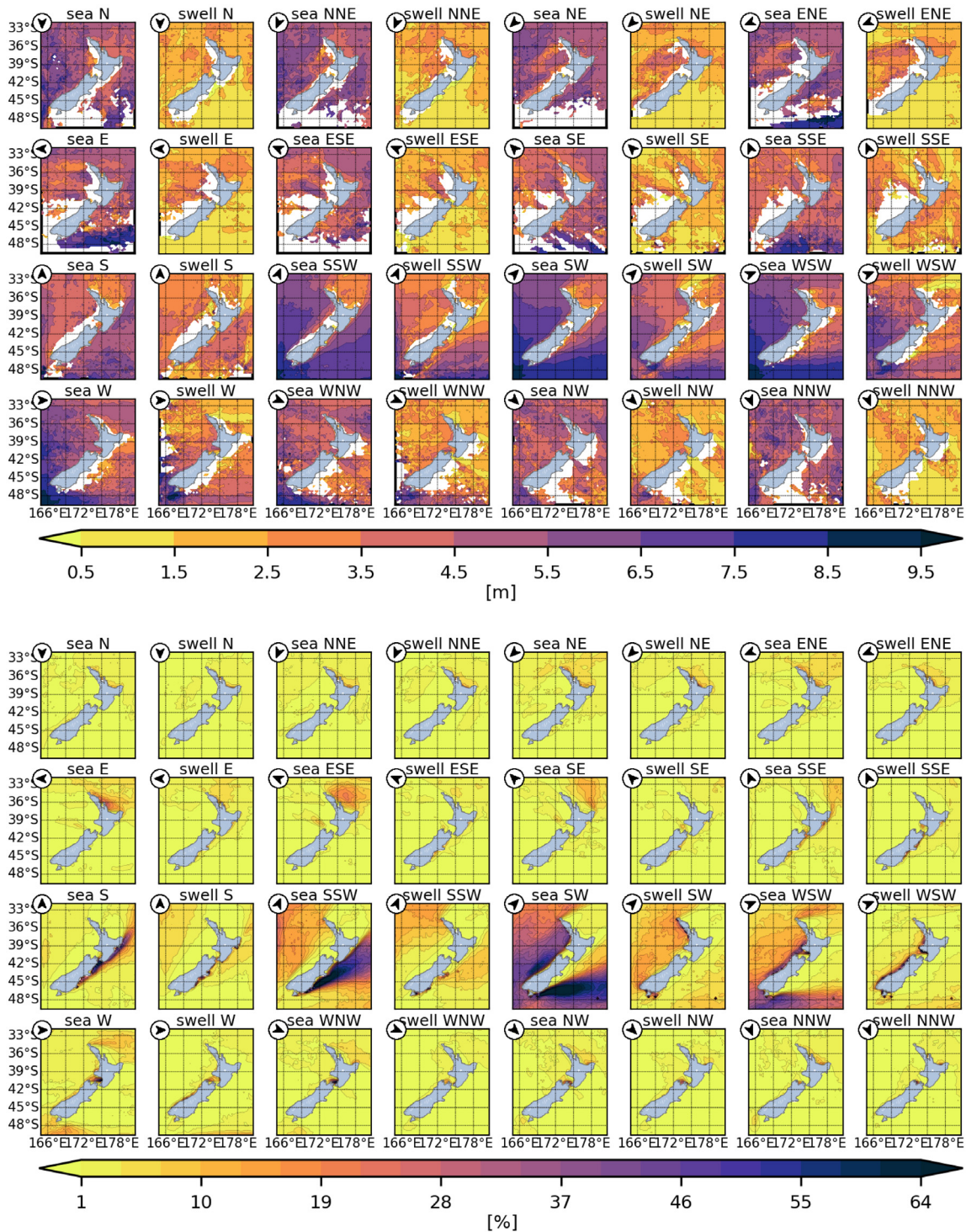


Fig. 12. Same as Fig. 11 but for wave heights during events of  $H_s^{99}$ . White areas represent zero values for  $H_s$  mean (top).

of the domain). During events of  $H_s^{99}$ , the wind-sea is responsible for ~75% (west coast) to 95% (southeast coast) of the total wave height while swells represent 5% to 25% of the remaining wave height (supplementary figure 2). Spatial patterns of wind-sea wave heights show a decreasing gradient northwards, which agrees with the decreasing gradient observed in the wind speed (left of supplementary figure 5) and the shadowing effects of New Zealand islands along the eastern coasts. Swell waves propagate longer, showing a more even wave height distribution along the country, which wraps New Zealand’s west and southeast coasts. Extreme events patterns show how the wind-sea

waves are more present along the south and southeast of New Zealand while swells become more present northwestwards. This agrees with the 99th percentile of wind speed plot (supplementary figure 5, right) as the largest wind speeds are along the south and southeast of New Zealand.

While the  $T_{m02}$  plot shows the distribution of higher frequencies of the wave spectrum in the study area, peak period of wind-sea waves shows the largest range of values and a different spatial distribution compared to swell waves. Along the west coast,  $T_{psea}$  values decrease

northwards while  $T_{pswells}$  nearly remains the same, which again demonstrates the connection between wind-sea waves and the predominant wind speed, i.e.,  $T_{psea}$  is larger where the winds are stronger. This also suggests wind-sea wave systems forced southwestwards of the study area detaching from the slower northern winds and being identified as swells as these waves propagate northeastwards. The increase in  $T_{psea}$  observed along the northwest coast of New Zealand suggests swell waves slowing down due to the bathymetry and being forced by the predominant westerlies (i.e., classified as wind-seas). Lower  $T_{psea}$  values throughout the eastern coasts show the blocking effects of New Zealand landmasses over the predominant (southwesterly) waves and winds, as well as the strong wind influence southwards of the South Island. Values of  $T_{pswells}$  are not as affected by New Zealand landmasses along the southeast coast since these waves propagate independently of the (blocked) winds. The difference between the  $T_{psea}$  and  $T_{pswells}$  values along the northeast coast is also related to the winds as the wind-sea waves along this coast are more likely to be generated by the predominant westerlies, as opposed to northeasterly waves, which will mostly be classified as swells.

The directional plots of wind-sea and swells presented are yet another source of information for the understanding of the wave systems throughout New Zealand waters, especially when supplemented by the plots of mean wave direction and mean swell direction (supplementary figure 6, left and right respectively). The wind-sea mean wave direction is strongly connected to the winds, however there is an evident northerly component on the wind-waves compared to the wind patterns along the study area (supplementary figure 5, left). Divergences are expected due to the different processes involved in the wave generation and propagation (nonlinear growth, quadruplet interactions, etc.), as well as the averaging of wind and wave directions. Wind-rose plots of 5 different points along the northwest (169.0°E, 33.0°S), northeast (178.0°E, 36.0°S), southwest (168.0°E, 41.0°S), southeast (46.5°S, 175.5°E) and south (169.0°E, 48.5°S) of the domain (supplementary figure 7) depict the actual variety of wind directions and speeds along the study domain, which explain such divergences.

Peak direction of swell waves shows spatial patterns very similar to the integrated peak direction and mean wave direction, which agrees with swell waves representing 60% to 80% of the total wave energy of the study area (supplementary figure 1). However, for mean swell wave directions (supplementary figure 6, right) a number of different wave systems can be identified throughout the study area, most of them not noticeable in the integrated mean direction plots or even identifiable by buoys<sup>2</sup>, especially for the west coast moorings.

The spatial distribution of such directions is averaged, hence the mean direction tends to be dominated by the most present wave system while the peak direction tends to be a balance between presence and energy of each wave system. Points of diverging peak (or mean) wave directions suggest locations where a certain wave system becomes dominant over the other and vice-versa, yet all wave systems are likely to coexist along the areas adjacent to these points. The most noticeable of such systems are the northern wave components off the southeast of the study area (supplementary figure 6, right), as well as the southeasterly systems northwest of the country. The seasonal changes in waves and winds cause a displacement of the diverging points, allowing a stronger northern component off the west coast to be identified during the summer months (right plot of supplementary figure 6).

Something the present analysis shows is how misleading the bulk parameters can be. In agreement with Portilla-Yandún (2018), wave direction is the most noticeable case where the aggregated value does not correspond to any of its components. Even with the use of partitioned data, the spatial distribution of swell parameters can still be misleading. The wind-sea, as the waves currently being forced by the winds,

<sup>2</sup> As only buoys that store spectral data are capable of providing information about such systems.

can be considered and consistently analyzed as a single wave system along the area it spreads through. This however cannot be applied to swells, as these systems tend to be spatially fragmented along different partitions according to their wave heights, and the aggregation of these wave systems into one partition implies loss of information. Therefore, conclusions based solely on the spatial distribution of aggregated swells are somehow still limited by averaging.

Regardless of their spatial characteristics however, partitions can be used to accurately define areas of crossing, opposing and following seas, using most of the conditions defined in previous studies, such as wave heights, periods, steepness and angle between systems. It is also possible to pinpoint these events in order to perform a closer inspection or check whether there are more than two simultaneous crossing, opposing or following wave systems during such events, or whether the wave systems involved are wind-sea and swells or only swells. As many of the crossing seas studies also consider stormy wave conditions, the changes in the spatial distribution of these seas during storm events also become important as the higher probability of their occurrence migrates from the south to the north of the study area.

Spatial patterns of MAV for aggregated wave height are similar to the ones in Godoi et al. (2016), however the values we found are 1% lower on the west and southeast coasts, and 6% along the northeast coast. The  $H_s$  IAV also shows values about 1.5% lower depending on the location, and a different spatial variability compared to Godoi et al. (2016). As the MAV analysis focuses on the variability that occurs within each year, the emerging spatial patterns are expected to be similar. However, whether the values differ between hindcasts depends on each hindcast's ability to reproduce the seasonal wave changes, which are tightly related to the seasonal changes in the wind forcings (small plots of supplementary figure 5, left). The IAV analysis is focused on the wave variability throughout the years and is likely to be affected by changes in the reanalysis observing systems, as well as changes in the atmospheric patterns/winds caused by anomalies in the atmospheric indices — both of which were different for the two databases, as each hindcast spans through different time frames with only a 9-year overlap. Wind-sea waves present larger mean annual variability west and southeast of New Zealand due to its exposure to westerly winds which, when present, are either generating waves or forcing the wave systems along the west coast. The MAV of wind-seas is also smaller along areas of strong and steady winds, such as off the Cook Strait, and south of the South Island. The smaller MAV along the northeast coast of New Zealand suggests windsea waves forced either by the westerlies or the trade winds depending on the season. Swell waves are more consistent throughout the whole domain year round, which reflects on the general lower values of MAV for swells, the largest occurring along areas where wind-seas are more present. For IAV, the interaction between winds and waves leading to such variabilities is similar to the ones described for MAV, however the drivers for these oscillations are the atmospheric indices. The variability observed in wind-sea waves is compatible with the north(south)-westerly and north(south)-easterly anomalies caused by the negative and positive phases of the atmospheric indices described in Section 2. Such variability suggests that the anomalies over the southwesterly winds imply larger wave oscillations than the ones related to easterly and northeasterly winds, and also reinforces the blocking effects of New Zealand landmasses over winds and waves throughout the eastern coasts. The noticeable IAV of swell waves along the west also indicates a stronger influence of the westerly anomalies over the easterly, which causes a smaller IAV to occur along the east coasts.

Winds and wave age/direction play an important role in the classification of wind-seas and swell waves. Therefore, it should be stressed that the model parametrizations (and potentially models' physics) can affect this classification even with a fixed value of the wave aging parameter ( $\beta$ ). A different approach was adopted by Portilla-Yandún (2018), who performed a time-series analysis of the spectral peaks and winds, which allowed him to identify the wave systems related to the



local winds. A comprehensive assessment on the impact of different values of  $\beta$  in partitioned parameters of different wave models, as well as in the wave climate analysis should be addressed in a future study.

Time series of seasonal/yearly mean of aggregated, wind-seas and swell wave heights at six sites throughout New Zealand has shown seasons where the mean wind-sea wave height was larger than the mean wave height (note that the mean wave height of swells and wind-seas here defined only accounts for sea states where  $H_{sea,swell} > 0$ ). This suggests few but high energy wind-sea events and steady smaller swells, the latter adding more weight to (i.e., decreasing) the mean wave height. A future study should explore the relationship between these large wind-seas, storms, and atmospheric indices.

The regression analysis over the wave height anomalies and the SOI along the west coast suggests that the waves (and winds) affected by this index are likely to decrease in intensity northwards, reaching sites *sw* and *w* as swells, while at site *nw* the changes only affect wind-seas. This is compatible with the equatorward shift of the westerly jet that occurs during El Niño events (Yang et al., 2018), and the consequent clockwise shift of swell wave directions (Hemer et al., 2010). The positive correlation between the SOI and  $H_{psea}^c$  at location *e* suggests the northeasterly anomaly in winds during La Niña events, yet no robust correlation was found at the other east coast sites. For the DMI, the correlation with  $H_{pswell}$  and  $H_{pswell}^c$  can be associated with the increase of cyclones frequency from 50°S to 75°S (and the decrease from 45°S to 65°S), as per Eichler and Gottschalck (2013). The correlation of the DMI with wind-seas at sites *w*, *sw* and *se* suggests some perturbation of the local winds, potentially due to the increased cyclone activity. Negative correlation of the SAM and wind-seas at all points along the west coast suggests the easterly (summer) and northeasterly (winter) anomalies that occur during the positive phases of SAM, which imply a reduction of the westerlies that would otherwise generate waves along these areas. Through the east coast, the SAM appears to influence only the northernmost points. However, as this index causes two different westerly anomalies in two different seasons, it is not straightforward to deduct which anomaly is affecting each point and wave type. For the SOI and SAM, robust correlation was found for wind-seas and swells, but not necessarily for the aggregated wave height, which shows the robustness of the partitioned analysis over the independent variability these systems can present. A future study analyzing the seasonal, spatial and directional correlation of partitioned waves and atmospheric anomalies is suggested to improve our understanding of the wave systems modulated by these indexes.

The sectoring approach is capable to depict accurately how the different wave systems interact with New Zealand's landmasses. In particular, the role of the Cook Strait in channeling winds (Harris, 1990) and generating waves that propagate northwestwards and southeastwards of it, creating crossing seas, as well as areas of more steady wind-seas. Another important feature shown by the directional plots for an area like New Zealand is the presence of wave systems propagating offshore or parallel to the coast. The  $\alpha$  plots for each sector show a non negligible wave height contribution for some of these systems, which are taken into account when calculating aggregated wave heights. This shows how the downscale of integrated parameters can potentially lead to hindcast inaccuracies due to the onshore propagation of offshore or cross-shore wave systems.

Future studies may use the sectorized data to explore what the actual incident wave height is along the coast, as well as to investigate the seasonality of each sector, and how they interfere in the aggregated wave parameters. Another potential application is to correlate the wave height of the directional sectors with atmospheric anomalies in order to find relationships that might not be detectable under the uni/bimodal representation of the wave spectrum. Finally, as the wave direction is of great importance on beach erosion and accretion (Harley et al., 2017; Short et al., 2001), the use of sectorized data could be explored by studies on beach morphodynamics, which usually only take into account integrated parameters.

## 6. Conclusion

This study presents a partitioned 20-year database of the New Zealand waters, downscaled at resolutions of 28 km and 9 km for the whole New Zealand, and 3 km and 1 km for three study areas, as well as locations of buoy deployments. The database was validated against 9 buoy moorings along the west, northeast and southeast coasts of the country.

A description of the wave climate of New Zealand based on integrated and partitioned parameters of wind-sea and swell waves was presented, and relationships between bulk parameters and partitions were identified. Areas of crossing, opposing, and following swells were defined around New Zealand, and the changes in these areas during storm events were also depicted. The inter annual and mean annual variability of integrated, wind-sea, and swell wave heights were also analyzed, and the importance of the wave aging parameter of the partitioning algorithm was emphasized. Time series of monthly wind-sea and swell wave height anomalies at six different locations along New Zealand were correlated with atmospheric indices. Partitions were rearranged into directional sectors of wind-sea and swell waves, for both mean and extreme wave heights. The directional sectors were analyzed in terms of mean and mean contribution.

The main findings of the present study are summarized below:

- The present database constitutes a reliable source of wave climate data for New Zealand, extending the current published wave climatology (15 years) and providing an extensive range of bulk and partitioned wave parameters.
- The validation shows good agreement with buoy data, suggesting improved skill of the present hindcast in reproducing the wave climate, compared to previous studies.
- The mean and  $\alpha$  analyses allowed us to assess the wave height and the energy share of wind-seas and swells in the total wave height.
- Swell direction analysis indicates wave systems not identifiable in integrated parameters or buoy data. The presence of such wave systems was confirmed and quantified by the directional sector analysis.
- The areas of crossing, opposing and following swells around New Zealand were identified for mean and extreme conditions.
- The differences in the inter annual variability of this and previous research are likely to be caused by changes in the reanalysis observing systems and anomalies in atmospheric indices that occurred during the different time-spans of each study.
- Inter and mean annual variabilities of wind-sea and swell waves are larger than inter and mean annual variability of integrated waves.
- The westerly anomalies of atmospheric indices have a higher impact on the wave climate than the easterly anomalies.
- The atmospheric indices correlated with time series of wave heights allowed us to identify robust correlations of the SAM and SOI for wind-seas and swells in locations where these indices do not correlate with the total wave height.

## CRediT authorship contribution statement

**João Albuquerque:** Conception and design of study, Acquisition of data, Analysis and/or interpretation of data, Writing – original draft. **Jose A.A. Antolínez:** Acquisition of data, Analysis and/or interpretation of data, Writing – review & editing. **Richard M. Gorman:** Writing – review & editing. **Fernando J. Méndez:** Conception and design of study, Acquisition of data, Writing – review & editing. **Giovanni Coco:** Conception and design of study, Writing – review & editing.



## Declaration of competing interest

The authors declare that they have no known competing financial interests or personal relationships that could have appeared to influence the work reported in this paper.

## Acknowledgments

The current research is funded by the now defunct New Zealand GNS-Hazard Platform through a grant to GC (contract 3710440). FJM acknowledges the Spanish Ministry of Science for the funding of project PID2019-107053RB-I00. All the programming code for this research was written in Python programming language ([www.python.org](http://www.python.org)), the SciPy python library (Virtanen et al., 2020) was used to solve the linear regression model and all the plots displayed (except for the windroses) were created with python's matplotlib module (Hunter, 2007). Finally, the authors wish to thank Fabrice Ardhuin for providing the IFREMER hindcast, Henrique Rapizo for providing the information about SWAN's patch version 41.31.A, and all the scientists who have contributed in building the databases used in the present study. Approval of the version of the manuscript to be published (João Albuquerque, Jose A.A. Antolín, Richard M. Gorman, Fernando J. Méndez and Giovanni Coco).

## Appendix A. Supplementary data

Supplementary material related to this article can be found online at <https://doi.org/10.1016/j.ocemod.2021.101897>.

## References

- Albuquerque, J.A., Antolín, J.A.A., Rueda, A., Méndez, F.J., Coco, G., 2018. Directional correction of modeled sea and swell wave heights using satellite altimeter data. *Ocean Model.* 131, 103–114. <http://dx.doi.org/10.1016/j.ocemod.2018.09.001>.
- Ashok, K., Nakamura, H., Yamagata, T., 2007. Impacts of ENSO and Indian Ocean dipole events on the Southern Hemisphere storm-track activity during austral winter. *J. Clim.* 20 (13), 3147–3163.
- Booij, N., Ris, R.C., Holthuijsen, L.H., 1999. A third-generation wave model for coastal regions: 1. Model description and validation. *J. Geophys. Res. Oceans* 104 (C4), 7649–7666.
- Caires, S., Sterl, A., Bidlot, J., Graham, N., Swail, V., 2004. Intercomparison of different wind-wave reanalyses. *J. Clim.* 17 (10), 1893–1913.
- Cavaleri, L., Bertotti, L., 2004. Accuracy of the modelled wind and wave fields in enclosed seas. *Tellus A* 56 (2), 167–175.
- Cavaleri, L., Sclavo, M., 2006. The calibration of wind and wave model data in the Mediterranean Sea. *Coast. Eng.* 53 (7), 613–627.
- Challenor, P., Woolf, D., Gommenginger, C., Srokosz, M., Cotton, D., Carter, D., Sykes, N., 2006. Satellite altimetry: A revolution in understanding the wave climate. In: *Proceedings of the Symposium on 15 Years of Progress in Radar Altimetry*. pp. 13–18.
- Chawla, A., Spindler, D.M., Tolman, H.L., 2013. Validation of a thirty year wave hindcast using the climate forecast system reanalysis winds. *Ocean Model.* 70, 189–206. <http://dx.doi.org/10.1016/j.ocemod.2012.07.005>, *Ocean Surface Waves*. URL <http://www.sciencedirect.com/science/article/pii/S1463500312001047>.
- Chen, W.Y., 1982. Assessment of southern oscillation sea-level pressure indices. *Mon. Weather Rev.* 110 (7), 800–807. [http://dx.doi.org/10.1175/1520-0493\(1982\)110<0800:AOSOSL>2.0.CO;2](http://dx.doi.org/10.1175/1520-0493(1982)110<0800:AOSOSL>2.0.CO;2), arXiv:[https://journals.ametsoc.org/mwr/article-pdf/110/7/800/4167557/1520-0493\(1982\)110\\_0800\\_aososl\\_2\\_0\\_co\\_2.pdf](https://journals.ametsoc.org/mwr/article-pdf/110/7/800/4167557/1520-0493(1982)110_0800_aososl_2_0_co_2.pdf).
- Coggins, J.H., Parsons, S., Schiel, D., 2015. An assessment of the ocean wave climate of New Zealand as represented in Kidson's synoptic types. *Int. J. Climatol.*
- Cox, A.T., Swail, V.R., 2001. A global wave hindcast over the period 1958–1997: validation and climate assessment. *J. Geophys. Res.* 106 (C2), 2313–2329.
- Diamond, H., Renwick, J., 2015. The climatological relationship between tropical cyclones in the southwest Pacific and the southern annular mode. *Int. J. Climatol.* 35 (4), 613–623.
- Eichler, T.P., Gottschalk, J., 2013. A comparison of Southern Hemisphere cyclone track climatology and interannual variability in coarse-gridded reanalysis datasets. *Adv. Meteorol.* 2013.
- Fauchereau, N., Pohl, B., Lorrey, A., 2016. Extratropical impacts of the Madden-Julian Oscillation over New Zealand from a weather regime perspective. *J. Clim.* 29 (6), 2161–2175.
- Godoi, V.A., Bryan, K.R., Gorman, R.M., 2016. Regional influence of climate patterns on the wave climate of the southwestern Pacific: The New Zealand region. *J. Geophys. Res. Oceans* 121 (6), 4056–4076. <http://dx.doi.org/10.1002/2015JC011572>.
- Godoi, V.A., Bryan, K.R., Stephens, S.A., Gorman, R.M., 2017. Extreme waves in New Zealand waters. *Ocean Model.* 117, 97–110. <http://dx.doi.org/10.1016/j.ocemod.2017.08.004>, URL <http://www.sciencedirect.com/science/article/pii/S146350031730118X>.
- Gong, D., Wang, S., 1999. Definition of antarctic oscillation index. *Geophys. Res. Lett.* 26, 459–462. <http://dx.doi.org/10.1029/1999GL900003>.
- Gordon, N.D., 1986. The southern oscillation and New Zealand weather. *Mon. Weather Rev.* 114 (2), 371–387.
- Gorman, R.M., Bryan, K.R., Laing, A.K., 2003a. Wave hindcast for the New Zealand region: Deep-water wave climate. *N. Z. J. Marine Freshwater Res.* 37 (3), 589–612.
- Gorman, R.M., Bryan, K.R., Laing, A.K., 2003b. Wave hindcast for the New Zealand region: nearshore validation and coastal wave climate. *N. Z. J. Marine Freshwater Res.* 37 (3), 567–588.
- Griffiths, G., 2011. Drivers of extreme daily rainfalls in New Zealand. *Weather Clim.* 31, 24–49.
- Grigorieva, V., Badulin, S., 2016. Wind wave characteristics based on visual observations and satellite altimetry. *Oceanology* 56 (1), 19–24.
- Hanson, J.L., Phillips, O.M., 2001. Automated analysis of ocean surface directional wave spectra. *J. Atmos. Ocean. Technol.* 18 (2), 277–293.
- Hanson, J.L., Tracy, B.A., Tolman, H.L., Scott, R.D., 2009. Pacific hindcast performance of three numerical wave models. *J. Atmos. Ocean. Technol.* 26 (8), 1614–1633.
- Harley, M.D., Turner, I.L., Kinsela, M.A., Middleton, J.H., Mumford, P.J., Splinter, K.D., Phillips, M.S., Simmons, J.A., Hanslow, D.J., Short, A.D., 2017. Extreme coastal erosion enhanced by anomalous extratropical storm wave direction. *Sci. Rep.* 7 (1), 1–9.
- Harris, T.F.W., 1990. Greater Cook Strait: Form and Flow. DSIR Marine and Freshwater.
- Hasselmann, K., Barnett, T., Bouws, E., Carlson, H., Cartwright, D., Enke, K., Ewing, J., Gienapp, H., Hasselmann, D., Kruseman, P., et al., 1973. Measurements of wind-wave growth and swell decay during the joint North Sea Wave Project (JONSWAP). *ErgÄnzungsheft* 8-12.
- Haver, S., Nyhus, K., 1986. A wave climate description for long term response calculations. In: *Fifth International Symposium on Offshore Mechanics and Arctic Engineering*, Vol. 4. Tokyo. p. 27.
- Hemer, M.A., Church, J.A., Hunter, J.R., 2010. Variability and trends in the directional wave climate of the Southern Hemisphere. *Int. J. Climatol. J. R. Meteorol. Soc.* 30 (4), 475–491.
- Hunter, J., 2007. Matplotlib: A 2D graphics environment. *Comput. Sci. Eng.* 9 (3), 90–95.
- Kidston, J., Renwick, J., McGregor, J., 2009. Hemispheric-scale seasonality of the southern annular mode and impacts on the climate of New Zealand. *J. Clim.* 22 (18), 4759–4770. <http://dx.doi.org/10.1175/2009JCLI2640.1>, arXiv:[https://journals.ametsoc.org/jcli/article-pdf/22/18/4759/3950726/2009jcli2640\\_1.pdf](https://journals.ametsoc.org/jcli/article-pdf/22/18/4759/3950726/2009jcli2640_1.pdf).
- Laing, A.K., 1993. Estimates of wave height data for New Zealand waters by numerical modelling. *N. Z. J. Marine Freshwater Res.* 27 (2), 157–175.
- Laing, A.K., 2000. New Zealand wave climate from satellite observations. *N. Z. J. Marine Freshwater Res.* 34 (4), 727–744.
- Lavidas, G., Venugopal, V., Friedrich, D., 2017. Sensitivity of a numerical wave model on wind re-analysis datasets. *Dyn. Atmos. Oceans* 77, 1–16.
- Mínguez, R., Espejo, A., Tomás, A., Méndez, F.J., Losada, I.J., 2011. Directional calibration of wave reanalysis databases using instrumental data. *J. Atmos. Ocean. Technol.* 28 (11), 1466–1485.
- Mitchell, J., Mackay, K., Neil, H., Mackay, E., Pallentin, A., Notman, P., 2012. Undersea New Zealand, 1:5,000,000. NIWA Chart, Miscellaneous Series 92.
- Pickrill, R., Mitchell, J., 1979. Ocean wave characteristics around New Zealand. *N. Z. J. Marine Freshwater Res.* 13 (4), 501–520.
- Portilla, J., Ocampo-Torres, F.J., Monbaliu, J., 2009. Spectral partitioning and identification of wind sea and swell. *J. Atmos. Ocean. Technol.* 26 (1), 107–122. <http://dx.doi.org/10.1175/2008JTECHO609.1>, arXiv:<https://doi.org/10.1175/2008JTECHO609.1>.
- Portilla-Yandún, J., 2018. The global signature of ocean wave spectra. *Geophys. Res. Lett.* 45 (1), 267–276. <http://dx.doi.org/10.1002/2017GL076431>, arXiv:<https://agupubs.onlinelibrary.wiley.com/doi/pdf/10.1002/2017GL076431>. URL <https://agupubs.onlinelibrary.wiley.com/doi/abs/10.1002/2017GL076431>.
- Rasche, N., Ardhuin, F., 2013. A global wave parameter database for geophysical applications. Part 2: Model validation with improved source term parameterization. *Ocean Model.* 70, 174–188.
- Rasche, N., Ardhuin, F., Queffelec, P., Croizé-Fillon, D., 2008. A global wave parameter database for geophysical applications. Part 1: Wave-current-turbulence interaction parameters for the open ocean based on traditional parameterizations. *Ocean Model.* 25 (3), 154–171.
- Reguero, B.G., Menéndez, M., Méndez, F.J., Mínguez, R., Losada, I.J., 2012. A global ocean wave (GOW) calibrated reanalysis from 1948 onwards. *Coast. Eng.* 65, 38–55.
- Rueda, A., Cagigal, L., Antolínez, J.A., Albuquerque, J.C., Castanedo, S., Coco, G., Méndez, F.J., 2019. Marine climate variability based on weather patterns for a complicated island setting: The New Zealand case. *Int. J. Climatol.* 39 (3), 1777–1786. <http://dx.doi.org/10.1002/joc.5912>.

- Rueda, A., Hegermiller, C.A., Antolínez, J.A., Camus, P., Vitousek, S., Ruggiero, P., Barnard, P.L., Erikson, L.H., Tomás, A., Mendez, F.J., 2017. Multiscale climate emulator of multimodal wave spectra: MUSCLE-spectra. *J. Geophys. Res. Oceans* 122 (2), 1400–1415.
- Saha, S., Moorthi, S., Pan, H.-L., Wu, X., Wang, J., Nadiga, S., Tripp, P., Kistler, R., Woollen, J., Behringer, D., Liu, H., Stokes, D., Grumbine, R., Gayno, G., Wang, J., Hou, Y.-T., Chuang, H.-y., Juang, H.-M.H., Sela, J., Iredell, M., Treadon, R., Kleist, D., Van Delst, P., Keyser, D., Derber, J., Ek, M., Meng, J., Wei, H., Yang, R., Lord, S., van den Dool, H., Kumar, A., Wang, W., Long, C., Chelliah, M., Xue, Y., Huang, B., Schemm, J.-K., Ebisuzaki, W., Lin, R., Xie, P., Chen, M., Zhou, S., Higgins, W., Zou, C.-Z., Liu, Q., Chen, Y., Han, Y., Cucurull, L., Reynolds, R.W., Rutledge, G., Goldberg, M., 2010. The NCEP climate forecast system reanalysis. *Bull. Am. Meteorol. Soc.* 91 (8), 1015–1058. <http://dx.doi.org/10.1175/2010BAMS3001.1>, arXiv:<https://doi.org/10.1175/2010BAMS3001.1>.
- Saha, S., Moorthi, S., Wu, X., Wang, J., Nadiga, S., Tripp, P., Behringer, D., Hou, Y.-T., Chuang, H.-y., Iredell, M., Ek, M., Meng, J., Yang, R., Mendez, M.P.n., van den Dool, H., Zhang, Q., Wang, W., Chen, M., Becker, E., 2014. The NCEP climate forecast system version 2. *J. Clim.* 27 (6), 2185–2208. <http://dx.doi.org/10.1175/JCLI-D-12-00823.1>, arXiv:<https://doi.org/10.1175/JCLI-D-12-00823.1>.
- Saji, N., Goswami, B., Vinayachandran, P., Yamagata, T., 1999. A dipole mode in the tropical Indian Ocean. *Nature* 401 (6751), 360–363.
- Semedo, A., 2018. Seasonal variability of wind sea and swell waves climate along the canary current: The local wind effect. *J. Marine Sci. Eng.* 6 (1), 28.
- Semedo, A., Saetra, Ø., Rutgersson, A., Kahma, K.K., Pettersson, H., 2009. Wave-induced wind in the marine boundary layer. *J. Atmos. Sci.* 66 (8), 2256–2271. <http://dx.doi.org/10.1175/2009JAS3018.1>, URL <https://journals.ametsoc.org/view/journals/atsc/66/8/2009jas3018.1.xml>.
- Semedo, A., Vettor, R., Breivik, Ø., Sterl, A., Reistad, M., Soares, C.G., Lima, D., 2015. The wind sea and swell waves climate in the nordic seas. *Ocean Dyn.* 65 (2), 223–240.
- Sepulveda, H.H., Queffelec, P., Ardhuin, F., 2015. Assessment of SARAL AltiKa wave height measurements relative to buoy, Jason-2 and Cryosat-2 data. *Marine Geodesy* 38 (S1), 449–465. <http://dx.doi.org/10.1080/01490419.2014.1000470>.
- Shanas, P., Kumar, V.S., Hithin, N., 2014. Comparison of gridded multi-mission and along-track mono-mission satellite altimetry wave heights with in situ near-shore buoy data. *Ocean Eng.* 83, 24–35.
- Short, A.D., Trembanis, A.C., Turner, I.L., 2001. Beach oscillation, rotation and the southern oscillation, Narrabeen beach, Australia. In: *Coastal Engineering 2000*. pp. 2439–2452.
- Snodgrass, F., Groves, G.W., Hasselmann, K., Miller, G., Munk, W., Powers, W., 1966. Propagation of ocean swell across the Pacific. *Phil. Trans. R. Soc. A* 259 (1103), 431–497.
- Støle-Hentschel, S., Trulsen, K., Borge, J.C.N., Olluri, S., 2020. Extreme wave statistics in combined and partitioned windsea and swell. *Water Waves* 1–16.
- Stopa, J.E., Ardhuin, F., Babanin, A., Zieger, S., 2016a. Comparison and validation of physical wave parameterizations in spectral wave models. *Ocean Model.* 103, 2–17.
- Stopa, J.E., Ardhuin, F., Babanin, A., Zieger, S., 2016b. Comparison and validation of physical wave parameterizations in spectral wave models. *Ocean Model.* 103, 2–17. <http://dx.doi.org/10.1016/j.ocemod.2015.09.003>, Waves and coastal, regional and global processes. URL <http://www.sciencedirect.com/science/article/pii/S1463500315001614>.
- Stopa, J.E., Cheung, K.F., Tolman, H.L., Chawla, A., 2013. Patterns and cycles in the climate forecast system reanalysis wind and wave data. *Ocean Model.* 70, 207–220.
- Toffoli, A., Bitner-Gregersen, E., Osborne, A.R., Serio, M., Monbaliu, J., Onorato, M., 2011. Extreme waves in random crossing seas: Laboratory experiments and numerical simulations. *Geophys. Res. Lett.* 38 (6).
- Toffoli, A., Lefèvre, J., Bitner-Gregersen, E., Monbaliu, J., 2005. Towards the identification of warning criteria: Analysis of a ship accident database. *Appl. Ocean Res.* 27 (6), 281–291. <http://dx.doi.org/10.1016/j.apor.2006.03.003>, URL <http://www.sciencedirect.com/science/article/pii/S0141118706000241>.
- Tolman, H.L., et al., 2009. User manual and system documentation of WAVEWATCH III TM version 3.14. In: *Technical Note, MMAB Contribution*, Vol. 276. p. 220.
- Torsethaugen, K., Faanes, T., Haver, S., 1984. characteristics for Extreme Sea States on the Norwegian Continental Shelf. Technical Report, (NHL 2 84123), Norwegian Hydrodynamics Laboratories, Division River and Harbour Laboratory, Trondheim, Norway.
- Tournadre, J., Lambin-Artru, J., Steunou, N., 2009. Cloud and rain effects on AltiKa/SARAL Ka-band radar altimeter—Part I: Modeling and mean annual data availability. *IEEE Trans. Geosci. Remote Sens.* 47 (6), 1806–1817.
- Violante-Carvalho, N., Parente, C.E., Robinson, I.S., Nunes, L.M.P., 2002. On the growth of wind-generated waves in a swell-dominated region in the south atlantic. *J. Offshore Mech. Arct. Eng.* 124 (1), 14–21.
- Virtanen, P., Gommers, R., Oliphant, T.E., Haberland, M., Reddy, T., Cournapeau, D., Burovski, E., Peterson, P., Weckesser, W., Bright, J., van der Walt, S.J., Brett, M., Wilson, J., Jarrod Millman, K., Mayorov, N., Nelson, A.R., Jones, E., Kern, R., Larson, E., Carey, C., Polat, I., Feng, Y., Moore, E.W., Vand erPlas, J., Laxalde, D., Perktold, J., Cimrman, R., Henriksen, I., Quintero, E., Harris, C.R., Archibald, A.M., Ribeiro, A.H., Pedregosa, F., van Mulbregt, P., Contributors, S., 2020. SciPy 1.0: Fundamental algorithms for scientific computing in Python. *Nature Methods* 17, 261–272. <http://dx.doi.org/10.1038/s41592-019-0686-2>.
- Vledder, G.v., Akpinar, A., 2017. Spectral partitioning and swells in the black sea. *Coast. Eng. Proc.* 1 (35), waves.21. <http://dx.doi.org/10.9753/icce.v35.waves.21>, URL <https://icce-ojs-tamu.tdl.org/icce/index.php/icce/article/view/8219>.
- Wang, D.W., Hwang, P.A., 2001. An operational method for separating wind sea and swell from ocean wave spectra. *J. Atmos. Ocean. Technol.* 18 (12), 2052–2062.
- Wentz, F.J., Ricciardulli, L., Hilburn, K., Mears, C., 2007. How much more rain will global warming bring? *Science* 317 (5835), 233–235.
- Yang, S., Li, Z., Yu, J.-Y., Hu, X., Dong, W., He, S., 2018. El Niño–Southern Oscillation and its impact in the changing climate. *Natl. Sci. Rev.* 5 (6), 840–857.
- Young, I., Vinoth, J., Zieger, S., Babanin, A.V., 2012. Investigation of trends in extreme value wave height and wind speed. *J. Geophys. Res. Oceans* 117 (C11).